Publication Year	2018
Acceptance in OA	2020-11-18T12:38:37Z
Title	Strong X-Ray and Multiwavelength Flaring Activity for 1ES 1959+650, 2016 August-2017 November
Authors	Kapanadze, B., Dorner, D., VERCELLONE, STEFANO, ROMANO, Patrizia, Hughes, P., Aller, M., Aller, H., Reynolds, M., Tabagari, L.
Publisher's version (DOI)	10.3847/1538-4365/aad8b5
Handle	http://hdl.handle.net/20.500.12386/28414
Journal	THE ASTROPHYSICAL JOURNAL SUPPLEMENT SERIES
Volume	238

The Astrophysical Journal Supplement Series, 238:13 (23pp), 2018 September https://doi.org/10.3847/1538-4365/aad8b5

Strong X-Ray and Multiwavelength Flaring Activity for 1ES 1959+650, 2016 August–2017 November

B. Kapanadze[1,2], D. Dorner[3], S. Vercellone[2], P. Romano[2], P. Hughes[4], M. Aller[4], H. Aller[4], M. Reynolds[4], and L. Tabagari[1]

[1] E. Kharadze Abastumani Astrophysical Observatory, Ilia State University, Colokashvili Av. 3/5, Tbilisi, D-0162, Georgia
[2] INAF, Osservatorio Astronomico di Brera, Via E. Bianchi 46, I-23807 Merate, Italy
[3] Universität Würzburg, Institute for Theoretical Physics and Astrophysics, Emil-Fischer-Str. 31, D-97074 Würzburg, Germany
[4] Astronomy Department, University of Michigan, Ann Arbor, MI 48109-1107, USA

Received 2018 June 23; revised 2018 July 31; accepted 2018 August 2; published 2018 September 26

Abstract

We present the detailed timing and spectral results obtained during the *Swift* observations of the TeV-detected blazar 1ES 1959+650 in 2016 August–2017 November. The source continued its trend of gradually enhancing X-ray flaring activity in the 0.3–10 keV energy range, starting in 2015 August, and a new highest historical brightness state was recorded twice. A long-term high state was superimposed by both weak and strong flares, and we detected 32 instances of intraday X-ray flux variability, including several occasions of extremely fast fluctuations with fractional amplitudes of 5.4%–7.5% within 1 ks exposures. The 0.3–10 keV spectra generally showed a best fit with the log-parabolic model, yielding a very wide range of the curvature parameter b and the photon index at 1 keV. The position of the synchrotron SED peak E_p showed an extreme variability on various timescales between energies less than 0.1 keV and 7.7 ± 0.7 keV, with 25% of the spectra peaking at hard X-rays. In 2017 May–November, the source mostly showed lower spectral curvature and an anticorrelation b–E_p, expected in the case of efficient stochastic acceleration of X-ray-emitting electrons. The 0.3–100 GeV and optical–UV fluxes also attained their highest historical values in this period, although the latter showed an anticorrelation with the 0.3–10 keV emission, which is explained by the stochastic acceleration of electrons with a narrow initial energy distribution, having an average energy significantly higher than the equilibrium energy.

Key words: BL Lacertae objects: individual (1ES 1959+650)

Supporting material: machine-readable tables

1. Introduction

Blazars constitute an extreme class of radio-loud active galactic nuclei (AGNs) in which a jet of magnetized plasma, closely aligned to our line of sight, is assumed to emanate with relativistic bulk velocity from the vicinity of a central supermassive black hole (SMBH; Abdo et al. 2011). BL Lacertae objects (BL Lacs), a blazar subclass, are widely accepted as the sources of strongly Doppler-boosted, non-thermal emission ranging from the radio to very high energy (VHE, $E \gtrsim 100$ GeV) γ-ray frequencies. This interpretation explains the observational features like weak or absent emission lines, compact and flat-spectrum radio emission, and superluminal motion of plasma blobs along the jet, as measured with radio interferometry (Falomo et al. 2014). BL Lacs are remarkable also with their strong flux variability across the whole electromagnetic spectrum, with timescales ranging from a few minutes (at X-ray and VHE γ-ray frequencies) to several years (the radio and optical domains). This property can provide us with important clues to the physics and structure of the innermost regions of BL Lacs, which are not accessible via direct observations. Therefore, they represent one of the favorite targets of the multi-wavelength (MWL) campaigns performed with various ground-based telescopes and space missions.

The $\log \nu$–$\log \nu F_\nu$ plane shows two different components in the spectral energy distribution (SED) of BL Lacs, extended over the radio-to-X-ray and MeV–TeV energy ranges, respectively. Due to the nonthermal, polarized nature of the lower-energy component, its origin is widely accepted as synchrotron emission of relativistic leptons. Depending on the position of the corresponding SED peak E_p, BL Lacs are broadly divided into two subclasses (see Padovani & Giommi 1995, and references therein): high-energy-peaked objects (HBLs, peaking at UV–X-ray frequencies) and low-energy-peaked objects (LBLs, with E_p presented in the infrared–optical part of the spectrum). Concerning the higher-energy component, the most frequently considered scenario incorporates an inverse Compton (IC) scattering of synchrotron photons by their "parent" electron–positron population (synchrotron self-Compton model, SSC; Marscher & Gear 1985, and references therein). However, this simple scenario sometimes is challenged by uncorrelated X-ray and TeV variability, as indicated by the observation of an "orphan" (i.e., not accompanied by the corresponding X-ray flare) TeV event in the typical HBL source 1ES 1959+650 (redshift $z = 0.048$; Krawczynski et al. 2004). A complicated, uncorrelated MWL variability can be more easily explained by multizone SSC scenario (Graff et al. 2008), external Compton (EC; Dermer et al. 1992), and hadronic processes (e.g., Mücke et al. 2003).

Since HBLs mostly present their synchrotron peaks at X-rays, they show significantly stronger and faster variability in this energy range than in lower-energy ones. Moreover, the X-ray emission is due to synchrotron radiation from the highest-energy electrons (according to the basic scenario), and the complex flux and spectral variability, observed in this band, may provide us with information about the injection and radiative evolution of freshly accelerated leptons/hadrons (since the typical radiative lifetimes are very short X-ray-emitting particles; see Massaro et al. 2004). Therefore, an intensive X-ray spectral/flux variability study of nearby bright HBLs, like 1ES 1959+650, can make a significant advance in our understanding of the physical processes at work in the vicinity of SMBHs and relativistic jets. Note that the intensive target-of-opportunity (ToO) observations with the X-ray Telescope (XRT; Burrows et al. 2005) on board *Swift* (Gehrels et al. 2004) revealed significantly enhanced X-ray flaring activity in this source compared to the previous years, which often showed a lack of the correlation with respect to the variability observed in other spectral bands (Kapanadze et al. 2016a, 2018a; Kaur et al. 2017; Patel et al. 2018).

In this paper, we report the results of the intensive *Swift*-XRT observations of 1ES 1959+650 during 2016 August–2017 November. Along with these data, we have analyzed the lower-energy data simultaneously obtained with the Ultraviolet/Optical Telescope (UVOT; Roming et al. 2005) on board the same satellite to draw conclusions about the target's long-term multiwavelength behavior and search for the interband cross-correlations. For the same purposes, we also constructed light curves for the same period using the publicly available data obtained with (i) the Burst Alert Telescope (BAT; Barthelmy et al. 2005) on board *Swift*, (ii) the Monitor of All Sky X-ray Image (MAXI; Matsuoka et al. 2009) device, (iii) the Large Area Telescope (LAT) on board *Fermi* (Atwood et al. 2009), (iv) the First G-APD Cherenkov Telescope (FACT; Anderhub et al. 2013), (v) the 40 m telescope of Owens Valley Radio Observatory (OVRO; Richards et al. 2011), and (vi) the long-term monitoring program MOJAVE (Lister et al. 2011).

The paper is organized as follows. Section 2 describes the data processing and analyzing procedures. In Section 3, we provide the spectral results. Those related to the MWL flux and spectral variability on diverse timescales are presented in Section 4. We discuss our results in Section 5. Finally, a summary and our conclusions are provided in Section 6.

2. Instruments, Observations, and Data Analysis

The source was targeted 93 times by the XRT during 2016 August 6 and 2017 November 12, mostly in the framework of the ToO observations of different urgencies triggered by us. The Level 1 XRT data were processed with the `XRTDAS` package developed at the ASI Science Data Center (ASDC) and distributed by HEASARC within the `HEASOFT` package (version 6.22.1). Since 1ES 1959+650 mostly was a very bright X-ray source in the period presented here, the XRT observed it only in the Windowed Timing (WT) mode. The event files were reduced, calibrated, and cleaned in the same way as reported in Kapanadze et al. (2018a). In the case of the pointing with ObsID 34588040 (2016 November 1, MJD 57,693), the image center of 1ES 1959+650 is just at the edge of the observational area, and the pixel with the highest count rate probably is outside of this area since the source showed an extreme dimming by a factor of about 6 in 0.6 days during this observation from the state corresponding to 20.4 counts s^{-1} and then brightened by a factor of 1.7 during the next 0.9-day interval. Therefore, this observation is not included in our study. The information about each XRT observation and the measurement results are provided in Table 1.[5]

Note that the timing and spectral results from the XRT observations with ObsID (340880)19–22 originally were published in Kapanadze et al. (2018a), although these observations turned out to be performed in the epoch of the first 0.3–10 keV flare reported in Section 4.3, and therefore the corresponding results are used for the analysis provided in this paper but not included in Tables 1–2 and 4.

The XRT observations were concentrated within two parts of the period presented here, denoted as Period 1 and Period 2 hereafter (see Table 3 for the corresponding date and MJD ranges). They were separated by the 3.5-month interval (when *Swift* did not target the source) and characterized by different spectral properties of 1ES 1959+650, along with a stronger X-ray flaring activity of the source in the latter period. Moreover, we have split each period into particular parts (Periods 1a–1c and 2a–2c, respectively; see Table 3), which were selected on the basis of short-term 0.3–10 keV flares occurring on timescales ranging from several days to a few weeks.

From the daily binned, 15–150 keV BAT count rates of 1ES 1959+650, obtained within the Hard X-ray Transient Monitor program[6] (Krimm et al. 2013), we selected only those corresponding to the detection with the recommended 5σ significance for the variability study. Additionally, we rebinned these data within time intervals of 1–2 weeks for the same purpose (with the `HEASOFT` tool `REBINGAUSSLC`). Using the online tool `MAXI ON-DEMAND PROCESS`, we extracted a 1-week binned light curve in the 2–6 keV band, which yielded the highest signal-to-noise ratios from the publicly available data provided by the MAXI team.[7] For the flux variability study, we used only those count rates corresponding to detections with a minimum significance of 5σ.

Simultaneously with the XRT, 1ES 1959+650 was observed with the UVOT, which is a Ritchey–Chretien optical system with a 30 cm mirror (Roming et al. 2005). The instrument cycled through each of the three optical (V, B, U) and three ultraviolet bands (*UVW1*, *UVM2*, *UVW2*), covering the wavelength range of 1700–6500 Å. The photometry and corrections on the Galactic absorption are done following the recipe provided in Kapanadze et al. (2018a). The corrected magnitudes and corresponding fluxes (in mJy) are presented in Table 2.

We retrieved the publicly available radio data from the website[8] of the OVRO 40 m telescope (Richards et al. 2011). The 15 GHz flux values, obtained under poor weather conditions and making sharp outliers from the historical light curve, were excluded from our study. Moreover, we have used the publicly available 15 GHz flux values provided at the MOJAVE website.[9]

The FACT telescope observed 1ES 1959+650 during 237 nights for a total of 591 hr in 2016 August–2017 November. For the variability study, we have used only the nightly binned TeV excess rates corresponding to detection significances higher than 3σ in nightly binning,[10] since more than 98% of these data are taken with a zenith distance small enough to not influence the energy threshold of the analysis significantly (see

---

[5] The three leading zeros of ObsIDs are omitted throughout the paper. The full versions of Tables 1, 2, 4, 9, and 10 are available online.

[6] See https://swift.gsfc.nasa.gov/results/transients/weak//1ES1959p650/.

[7] http://maxi.riken.jp/

[8] See http://www.astro.caltech.edu/ovroblazars/.

[9] http://www.physics.purdue.edu/astro/MOJAVE/sourcepages//1959+650.shtml

[10] See http://www.fact-project.org/monitoring/.

Table 1
The XRT Observations of 1ES 1959+650 in 2016 August–2017 November

ObsID (1)	Obs. Start–End (UTC) (2)	Exposure (s) (3)	MJD (4)	CR (counts s^{-1}) (5)	χ_r^2/dof (6)	Bin (s) (7)	Var. (8)
34588023	2016 Aug 18 05:25:58 Aug 18 18:59:36	1539	57,618.23	9.19(0.09)	152.68/1	Or	V
34588024	2016 Aug 21 04:51:58 Aug 21 06:03:11	1349	57,621.21	5.41(0.09)	2.56/10	60 s	PV
34588025	2016 Aug 31 18:58:58 Aug 31 20:05:22	1020	57,631.79	7.45(0.12)	2.50/16	60 s	V

Note. The columns are as follows: (1) observation ID; (2) its start and end times (in UTC); (3) exposure (in s); (4) Modified Julian Date of the observation start; (5): mean value of the 0.3–10 keV count rate (CR, in counts s^{-1}) and its error shown within parentheses, similar to the quantities presented in the next tables; (6) reduced χ^2 with corresponding dof; (7) time bin; (8) existence of a flux variability (V: variable; PV: possibly variable; NV: nonvariable).

(This table is available in its entirety in machine-readable form.)

Dorner et al. 2015, for the analysis details). More than 90% of the same data are taken under light conditions not increasing the analysis threshold. This results in 19 nights for which the nightly observation time ranges from 2.5 to 4.7 hr. Finally, see Kapanadze et al. (2018a) for the LAT data processing and extraction of 300 MeV–100 GeV photon flux and spectral information for our target.

3. Results from the Spectral Analysis

3.1. Fitting Procedure

We performed the 0.3–10 keV spectral analysis using the `XSPEC` package (integrated within `HEASOFT`). For this purpose, the latest response matrix from the *Swift*-CALDB and ancillary response files (ARFs) were adopted. The latter were generated by means of the `XRTMKARF` task to account for the point-spread function losses, different extraction regions, vignetting, and CCD defects. The instrumental channels were combined to include at least 20 photons per bin using the task `GRPPHA` (for making the spectrum valid for the χ^2-statistics).

The 0.3–10 keV spectra were fitted by fixing the hydrogen column density to the Galactic value $N_H = 1.00 \times 10^{21}$ cm^{-2} (Kalberla et al. 2005). However, we also performed the analysis setting N_H as a free parameter, similar to Aliu et al. (2013, 2014), or due to possible additional absorption reported by Fumagalli et al. (2012) and Furniss et al. (2013). However, its best-fit values from different spectra were close (larger or smaller in the particular cases) to the Galactic value provided by Kalberla et al. (2005), with the values of the spectral parameters being within the error ranges of those obtained during the fit with the fixed N_H. Nevertheless, the uncertainties related to the values of different spectral parameters are 3–5 times lower when performing the analysis with the fixed column density. Therefore, the results obtained for the fixed N_H are presented in this paper and used for the further analysis.

First of all, the spectra were fitted with the log-parabolic model $F(E) = K(E/E_1)^{-(a+b\log(E/E_1))}$ (Massaro et al. 2004), with $E_1 = 1$ keV, a the photon index at the energy E_1, b the curvature parameter, and K the normalization factor. However, we also checked the validity of a simple power law $F(E) = KE^{-\Gamma}$ (Γ, the photon index throughout 0.3–10 keV energy range) and broken power law[11] for each spectrum (using the reduced chi-squared [χ_r^2], distribution of the residuals, and F-test). We generated spectra from separate orbits of the particular XRT observation when (i) it was impossible to use the same source and/or background extraction regions for all orbits that were shifted with respect to each other, or (ii) the source showed a flux variability during this observation. The same method was applied even to the single orbit when the flux varied within it, or when there was no satisfactory fit with any model for the spectrum corresponding to the whole orbit, and we extracted the spectra from its separate segments.

After the best-fit model selection and derivation of the values of different spectral parameters, the task `EDITMOD` was used to remove the absorption component in order to measure de-absorbed 0.3–2 keV, 2–10 keV, and 0.3–10 keV fluxes and the associated errors (in logarithmic units). The hardness ratio (HR) was calculated as $\mathrm{HR} = F_{2-10\,\mathrm{keV}}/F_{0.3-2\,\mathrm{keV}}$, where the symbols $F_{2-10\,\mathrm{keV}}$ and $F_{0.3-2\,\mathrm{keV}}$ denote the de-absorbed 2–10 keV and 0.3–2 keV fluxes, respectively.

For the vast majority of the spectra (168 out of 170), simple and broken power-law models were excluded at the 99.99% confidence level, showing trends in the fit residuals and unacceptable values of χ_r^2, while the log-parabolic model yielded a significantly better fit according to these tests. The corresponding results are provided in Table 4. Only two spectra from the period presented here do not show a significant curvature and are fitted well with a simple power law (see Table 5). In Table 6, we present the properties of the distribution of the spectral parameters for the whole 2016 August–2017 November period and for its separate parts (Periods 1 and 2).

3.2. Spectral Curvature

A good log-parabolic fit of the aforementioned 168 spectra indicate the presence of significant spectral curvature in each. The curvature parameter b showed a very broad range of the values between $b = 0.10 \pm 0.05$ and $b = 0.83 \pm 0.12$ (Figure 1(Aa)). Note that the spectra from Period 1 generally show larger curvature than those from Period 2: the weighted mean value of the curvature parameter $\bar{b} = 0.47 \pm 0.01$,[12] and 63% of the values are larger than $b = 0.40$ (a conventional threshold between the relatively higher and lower curvatures) in this period, while 58% of spectra from Period 2 showed the curvatures below this threshold and $\bar{b} = 0.36 \pm 0.02$ (see Figures 1(Ab)–(Ac) and Table 6). Among different parts of these periods, on average, the spectra from Period 1c show the largest curvatures ($\bar{b} = 0.54 \pm 0.02$), while Period 2b was

---

[11] See https://heasarc.gsfc.nasa.gov/xanadu/xspec/manual//XSmodelBknpower.html for details.

[12] The difference between the distributions of the parameter b in Periods 1 and 2 was confirmed by means of the Kolmogorov–Smirnov (K-S) test at the 99% confidence level. The same test was used when comparing the distributions of other spectral parameters in different periods (reported below). The weighted mean values of different parameters are reported throughout the paper.

Table 2
The Results of the UVOT Observations

	V		*B*		*U*		*UVW1*		*UVM2*		*UVW2*	
ObsID	Mag.	Flux	Mag.	Flux	Mag.	Flux	Mag.	Flux	Mag.	Flux	Mag.	Flux
34588023	14.06(0.05)	8.71(0.41)	14.40(0.04)	7.05(0.24)	13.50(0.04)	5.75(0.22)	13.39(0.05)	3.91(0.19)	13.14(0.05)	4.25(0.14)	13.26(0.04)	3.66(0.11)
34588024	14.01(0.03)	9.12(0.29)	14.34(0.03)	7.45(0.17)	13.45(0.03)	6.03(0.18)	13.36(0.04)	4.02(0.15)	13.18(0.04)	4.09(0.11)	13.20(0.03)	3.87(0.14)
34588025	14.20(0.04)	7.66(0.29)	14.53(0.04)	6.25(0.17)	13.58(0.04)	5.35(0.18)	13.50(0.04)	3.53(0.15)	13.36(0.04)	3.47(0.11)	13.45(0.04)	3.08(0.11)

Note. The flux values in each band are given in units of mJy.

(This table is available in its entirety in machine-readable form.)

Table 3
The Periods and Subperiods Referred to throughout the Paper

Period	Dates	MJD
1	2016 Aug 6–2017 Feb 13	57,606–57,797
1a	2016 Aug 6–Oct 9	57,606–57,670
1b	2016 Oct 21–Dec 18	57,682–57,740
1c	2016 Dec 21–2017 Feb 13	57,740–57,797
2	2017 May 27–Nov 12	57,900–58,070
2a	2017 May 27–Jul 22	57,900–57,956
2b	2017 Jul 25–Sep 25	57,959–58,021
2c	2017 Oct 7–Nov 12	58,033–58,070

characterized by smallest curvatures ($\bar{b} = 0.33 \pm 0.01$). In Period 1, the source exhibited a significantly larger fraction of the spectra showing the curvature larger than $b_* = 0.55$ (21% of all curved spectra from this period; see Section 5.1 for the definition of b_* and the corresponding discussion).

The values of the parameter b from the whole period 2016 August–2017 November showed a weak anticorrelation[13] with the position of the synchrotron SED peak $E_{\rm p}$ (see Figure 2(Aa) and Table 7 for the value of the Spearman correlation coefficient and the corresponding p-value). However, this trend was present only in Period 2, while the source did not exhibit a significant b–$E_{\rm p}$ correlation in the previous period (Figures 2(Ab)–(Ac)). The curvature parameter showed a very weak positive correlation at the 99% confidence level with the photon index at 1 keV during 2016 August–2017 November (see Section 5.1 for the discussion). Finally, the parameter b showed an anticorrelation with the de-absorbed 0.3–10 keV flux in Period 1 (Figure 2(C)).

3.3. Photon Index and HR

Similar to the parameter b, the photon index at 1 keV showed a very wide range in the period presented here, with $\Delta a = 0.86$ and the hardest spectrum described with $a_{\rm min} = 1.55 \pm 0.03$. A total of 69% of the spectra showed $a < 2$ (when the spectrum is considered to be hard; Costamante et al. 2018; see Figure 1(Ba)). On average, Period 2 was characterized by harder spectra compared to the previous period: 78% of the spectra showing $a < 2$ and the mean value $\bar{a} = 1.83 \pm 0.03$ versus 52% and $\bar{a} = 2.00 \pm 0.03$ in Period 1. Nevertheless, the skewness of the distribution of parameter a is positive (i.e., shifted toward lower values) and 3 times larger in Period 2 than that associated with the spectra from Period 1. On average, the spectra were the hardest in Period 2b ($\bar{a} = 1.72 \pm 0.01$), while Period 1c was characterized by the softest spectra ($\bar{a} = 2.17 \pm 0.02$).

Similar to previous years, the source followed a "harder-when-brighter" spectral trend during X-ray flares in 2016 August–2017 November (Figure 2(C)). As for the particular subperiods, on average, the highest and lowest fluxes belong to Periods 2b and 1c, which showed the hardest and softest spectra, respectively.

The values of HR showed a wide range $\Delta{\rm HR} = 1.02 \pm 0.05$ in 2016 August–2017 November (see Tables 4 and 5 and Figure 1(C)). Note that 18% of the values are larger than HR = 1 (when the hard 2–10 keV flux is higher than the soft 0.3–2 keV flux: observed rarely in HBLs, where the contribution from IC photons to the hard X-ray range is negligible), and all these are derived from the spectra belonging to Period 2. The scatter plot HR–$F_{0.3-10{\rm keV}}$, constructed for the whole period 2016 August–2017 November, as well as for its separate parts, confirms the dominance of the aforementioned "harder-when-brighter" -spectral evolution of our target during X-ray flares (see Figure 2(E) and Table 7).

3.4. The Position of the Synchrotron SED Peak

Using the best-fit values of the parameters a and b, we calculated the position of the synchrotron SED peak as (Massaro et al. 2004) $E_{\rm p} = E_1 10^{(2-a)/2b}$ keV, which showed a very wide range between $E_{\rm p} = 0.17 \pm 0.05$ keV and $E_{\rm p} = 7.74 \pm 0.72$ keV. However, we checked that the SED peaks of the spectra with $E_{\rm p} \lesssim 0.5$ keV (6% of all log-parabolic-spectra) are poorly constrained by the observational data, and the corresponding $E_{\rm p}$ values are shifted to higher energies with respect to those obtained from the fit of contemporaneous broadband SEDs with the log-parabolic function $\log \nu F_\nu = A(\log \nu)^2 + B(\log \nu) + C$ (Landau et al. 1986), and these shifts are larger than the uncertainties associated with $E_{\rm p}$. Therefore, these values $E_{\rm p} < 0.5$ keV should be considered as upper limits. Moreover, Figure 3 presents the 0.3–10 keV SEDs of six spectra with $E_{\rm p} > 5$ keV, demonstrating that the SED peaks in Figures 3(a) and (c)–(f) ($E_{\rm p} = 6.54$–7.74 keV) also are relatively poorly constrained with the observational data, and the intrinsic positions of the peaks, obtained from the broadband fit, are systematically smaller than the $E_{\rm p}$ values derived from the spectral analysis. However, these differences are not larger than the associated errors (amounting to 0.47–0.72 keV; see Table 4).

Note that Period 2 was characterized by higher values of $E_{\rm p}$ than the previous period. Namely, all the spectra with $E_{\rm p} > 5$ keV and 41 out of 42 spectra with $E_{\rm p} > 2$ keV (i.e., hard X-ray peaking ones, taking the error ranges into account) belong to this period (see Table 6 and Figure 1(D)). In contrast, only one spectrum from Period 1 shows its synchrotron SED peak at hard X-rays, and the period-averaged value of $E_{\rm p}$ was two times smaller than in Period 2. This parameter shows a positive correlation with the 0.3–10 keV flux, which was stronger in Period 2 than in Period 1 (see Figure 2(F) and Table 7).

4. Flux and Spectral Variability

4.1. Long-term Flux Variability

Figure 4(a) presents a historical 0.3–10 keV light curve of 1ES 1959+650, which demonstrates a phase of significantly enhanced X-ray activity of the source since 2015 August.[14] Note that this activity becomes gradually stronger with time: the mean 0.3–10 keV count rate ($\overline{\rm CR}$) was 10.30 ± 0.01 counts s^{-1} during 2015 August–2016 February (Kapanadze et al. 2016a), it increased by 13% during 2016 February 1–July 31 (Kapanadze et al. 2018a), and it attained the value $\overline{\rm CR} = 14.55 \pm 0.01$ counts s^{-1} in the period presented here.[15] During the 3.4 yr period, a new highest historical 0.3–10 keV rate was recorded 6 times, occurring twice

---

[13] All significant correlations, reported throughout the paper, are detected above the 99% confidence level; consequently, each correlation is mentioned as very strong, strong, moderate, weak, or very weak when the corresponding Spearman coefficient showed a value of $\rho > 0.9$, $0.7 < \rho < 0.9$, $0.5 < \rho < 0.7$, $0.3 < \rho < 0.5$, or $0.2 < \rho < 0.3$, respectively.

[14] The flux variability in different spectral bands is reported at the 99.9% confidence level (unless otherwise stated), checked by means of the χ^2-test.

[15] A similar increase is observed also in the case of the de-absorbed 0.3–10 keV flux.

Table 4
Results of the Spectral Analysis with the Log-parabolic Model

ObsId (1)	a (2)	b (3)	E_p (4)	100 × K (5)	χ^2_r/dof (6)	$F_{0.3-2\ \mathrm{keV}}$ (7)	$F_{2-10\ \mathrm{keV}}$ (8)	$F_{0.3-10\ \mathrm{keV}}$ (9)	HR (10)
34588023 Or1	2.07(0.05)	0.36(0.09)	0.80(0.10)	6.10(0.14)	0.91/131	17.86(0.53)	9.89(0.51)	27.73(0.76)	0.55(0.03)
34588023 Or2	1.88(0.05)	0.18(0.06)	2.15(0.22)	6.92(0.10)	0.98/245	19.86(0.36)	17.74(0.52)	37.58(0.69)	0.89(0.03)
34588024	1.68(0.07)	0.45(0.12)	2.27(0.32)	3.35(0.09)	1.02/171	8.97(0.34)	8.77(0.43)	17.74(0.60)	0.98(0.06)

Note. The E_p values (Col. (4)) are given in keV; de-absorbed 0.3–2 keV, 2–10 keV, and 0.3–10 keV fluxes (Cols. (7)–(9)) are given in 10^{-11} erg cm^{-2} s^{-1}.
(This table is available in its entirety in machine-readable form.)

Table 5
The Results of the XRT Spectral Analysis with a Simple Power-law Model

ObsId (1)	Γ (2)	100 × K (3)	χ^2_r/dof (4)	$F_{0.3-2\ \mathrm{keV}}$ (5)	$F_{2-10\ \mathrm{keV}}$ (6)	$F_{0.3-10\ \mathrm{keV}}$ (7)	HR (8)
34588026 Orbit 1	2.18(0.03)	4.06(0.08)	0.94/132	12.97(0.32)	8.09(0.34)	21.09(0.39)	0.62(0.03)
93251002 Orbit 1	1.93(0.05)	11.49(0.46)	1.02/80	34.36(1.62)	32.96(2.36)	67.3(2.44)	0.96(0.07)

Note. De-absorbed 0.3–2 keV, 2–10 keV, and 0.3–10 keV fluxes (Cols. (5)–(7)) are given in 10^{-11} erg cm^{-2} s^{-1}.

Table 6
Distribution of Spectral Parameters in Different Periods (Excluding the Detections below the 3σ Significance and Upper Limits)

Quantity	Min. Value	Max. Value	Mean Value	Skewness
		2016 Aug–2017 Nov		
b	0.15(0.05)	0.83(0.12)	0.41(0.02)	0.62
a	1.55(0.03)	2.41(0.02)	1.90(0.03)	0.23
E_p	0.50(0.06)	7.74(0.72)	1.86(0.33)	2.20
HR	0.27(0.01)	1.29(0.05)	0.75(0.05)	0.23
		Period 1		
b	0.18(0.06)	0.83(0.12)	0.47(0.01)	0.41
a	1.56(0.04)	2.41(0.02)	2.00(0.03)	0.13
E_p	0.50(0.06)	2.27	1.16(0.19)	0.58
HR	0.27(0.01)	0.98(0.04)	0.61(0.06)	0.01
		Period 2		
b	0.15(0.05)	0.72(0.07)	0.36(0.02)	0.45
a	1.55(0.03)	2.33(0.03)	1.83(0.03)	0.42
E_p	0.52(0.07)	7.74(0.72)	2.32(0.42)	1.69
HR	0.37(0.02)	1.29(0.05)	0.85(0.05)	−0.04

during 2016 August–2017 November. The latest highest level (recorded on 2017 September 12, MJD 58,008.96) reached 39.18 ± 0.26 counts s^{-1}, which was 58% higher than that recorded before 2016 August (and reported in Kapanadze et al. 2018a).

Note also that Period 2 was characterized by higher X-ray brightness compared to the previous period: the mean 0.3–10 keV rate was 18.67 ± 0.01 counts s^{-1} versus $\overline{\mathrm{CR}} = 10.72 \pm 0.01$ counts s^{-1} from Period 1, i.e., on average, the source was fainter during Period 1 compared to the periods 2016 June–July and 2017 May–November. The maximum-to-minimum ratio of the de-absorbed 0.3–10 keV flux R was equal to 4.6 and 9.3[16] in Periods 1 and 2, respectively. In each period, the source showed several X-ray flares on timescales from several days to a few weeks, which are discussed in detail in Section 4.3.

In 2009–2017, 1ES 1959+650 was detected 138 times in the 2–6 keV band by *MAXI* with 5σ significance from 1-week binned observations (see Figure 4(b)). The source showed a flare in Period 2 that was stronger than that recorded in 2016 June–July. However, the source was very faint in the 15–150 keV energy range, similar to previous years, and it was detected only 6 times with 5σ significance from the daily binned BAT observations in the period presented here, which did not reveal significant flaring activity (Figure 4(c)).

In contrast to the activity in 2016 June–July (MJD 57,540–57,600; see Figure 4(d) and Kapanadze et al. 2018a), 1ES 1959+650 did not show a significant VHE flaring activity from the FACT excess rates corresponding to the 19 detections with 3σ significance from the daily binned data in the period presented here. Note, however, that the source was observed only once during 2016 December 16–2017 April 20, when it showed at least two strong X-ray flares (see Section 4.3), and the aforementioned detections were concentrated in the time intervals 2016 August 21–September 12 (lower X-ray states) and 2017 August 16–October 22 (coinciding with higher X-ray states or strong X-ray flares).

In 2015 May, 1ES 1959+650 underwent a long-term HE flare, lasting about 9 months, and has kept a general higher 0.3–100 GeV state since that epoch (compared to previous years, except for a fast "spike" centered on MJD 56,667, 2014 January), superimposed by relatively fast, strong flares in some time intervals (Figure 4(e)). In 2017 July, the source showed its highest 0.3–100 GeV state, exceeding a level of 10^{-7} photons cm^{-2} s^{-1} in the case of 2-week bins (although it showed a similar state earlier, in 2015 October, with 1-week binned observations). Moreover, the source was mostly detectable with the 3D binned LAT data above the 3σ threshold in the period presented here (in contrast to the epoch before 2015 May), exhibiting a flaring activity on various timescales.

Although the source showed a significantly weaker and slower variability with the maximum-to-minimum flux ratio R = 1.9(0.3)–2.1(0.3) in the ultraviolet *UVW1–UVW2* and optical *V–U* bands with R = 2.1(0.5)–2.7(0.4) during 2016 August–2017 November, it attained a new highest historical

---

[16] The errors associated with the variability factors during the XRT-band flares in 1ES 1959+650 on timescales from several days to a few weeks and maximum-to-minimum flux ratios, presented in this paper, generally are of order of 0.2 for both the 0.3–10 keV count rate and de-absorbed flux.

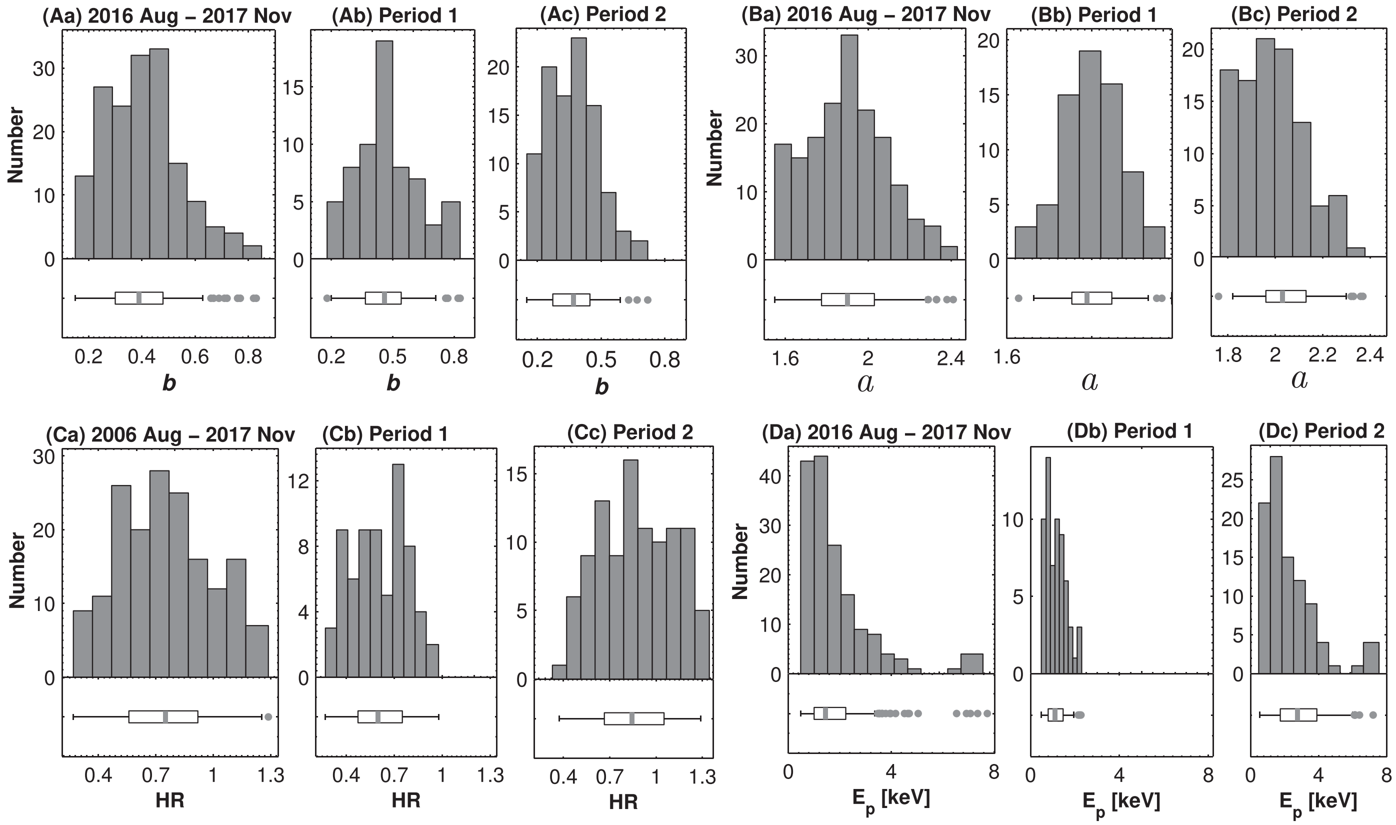

Figure 1. Distribution of the values of spectral parameters in different periods. A gray line within each panel corresponds to the median of the distribution, and the gray points represent the outliers. The whisker length equals the interquartile range.

brightness state in all bands on MJD 57,743 (Period 1) and MJD 58,061 (Period 2; see Figures 4(f) and (g)). On average, 1ES 1959+650 also showed elevated radio-band states during the OVRO and MOJAVE observations during 2016 August–2017 November, with its highest 15 GHz state for the period 2015–2017 recoded on MJD 58,059 (in the epoch of the highest optical–UV states; Figure 4(h)). Note also that the source is showing a gradually rising baseline radio flux with time. However, the radio variability was much weaker and slower with the maximum-to-minimum flux ratio $R = 1.31$ (0.3) compared to that observed in the higher-energy bands.

4.2. Spectral Variability

The photon index at 1 keV was highly variable in both Periods 1 and 2 on diverse timescales with the ranges $\Delta a = 0.84(0.04)$ and $\Delta a = 0.78(0.04)$, respectively. The largest hardenings by $\Delta a = 0.56$–0.67 were recorded along with the 0.3–10 keV flares (during MJD 57,700.4–57,711.6, 57,916.6–57,928.0, and 57,956.3–57,975.1; Figures 5(a)–(f)). However, the source showed an exclusion from the general "harder-when-brighter" trend during some short time intervals: the spectrum softened during MJD 57,670.3–57,682.7 and 57,741.0–57,743.1, when the brightness increased by a factor of 1.4–1.6. As for the opposite trend, the largest softenings by $\Delta a = 0.50$–0.56 occurred along with the large brightness declines by a factor of 3.7–8.2 during MJD 57,734.4–57,740.4 and 58,052.0–58,070.0. The photon index was variable by $\Delta a = 0.08$–0.38 on intraday timescales, generally associated with intraday variability (IDV; see Section 4.3 and Table 9 for details). However, this variability was not observed on subhour timescales, in contrast to the period 2016 February–July (Kapanadze et al. 2018a). In the period presented here, the fastest spectral variability included was a softening by $\Delta a = 0.19(0.04)$ in 1.64 hr (on MJD 57,900).

The hardness ratio also varied on various timescales and showed the largest increases by a factor of 2.2–2.6 and drops by a factor of 2.7–2.9 during the aforementioned strongest changes of the photon index (with the uncertainties of ~0.4; see Figures 5(a)–(f)). This quantity also varied by 17%–77% on intraday timescales (along with 0.3–10 keV IDVs; see the last column of Table 9).

The parameter b showed changes by $\Delta b = 0.15$–0.39 during several 0.3–10 keV IDVs, with the most extreme instance including an increase by $\Delta b = 0.20(0.09)$ during the aforementioned fastest variability of the photon index. On longer timescales, the spectral curvature showed the largest increase by $\Delta b = 0.53$ during MJD 58,022.0–58,033.0, while it declined by $\Delta b = 0.49$–0.59 in 2.9–12.0 days along with the 0.3–10 keV flares (Figures 5(a)–(f)).

Finally, the position of the synchrotron SED peak underwent shifts by 0.9–6.1 keV in 3.0–17.6 days toward higher frequencies, and the opposite trend by 0.8–5.6 keV in 4.0–18.0 days was also observed (Figures 5(a)–(f)). Generally, the parameter E_p showed a positive correlation with the 0.3–10 keV flux during these events (i.e., shifting to higher energies with increasing brightness, and moving back to lower energies as the source was becoming fainter; see also Figures 5(a)–(f)). Note that these variations were the largest in Period 2 (during MJD 57,968–58,022). However, it showed an increase by 4.4 (0.7) keV in 1.26 days and then declined by 5.2(0.6) keV during MJD 58,020.38–58,021.66, while the 0.3–10 keV flux did not show a significant variability (Figure 5(e)). Except for

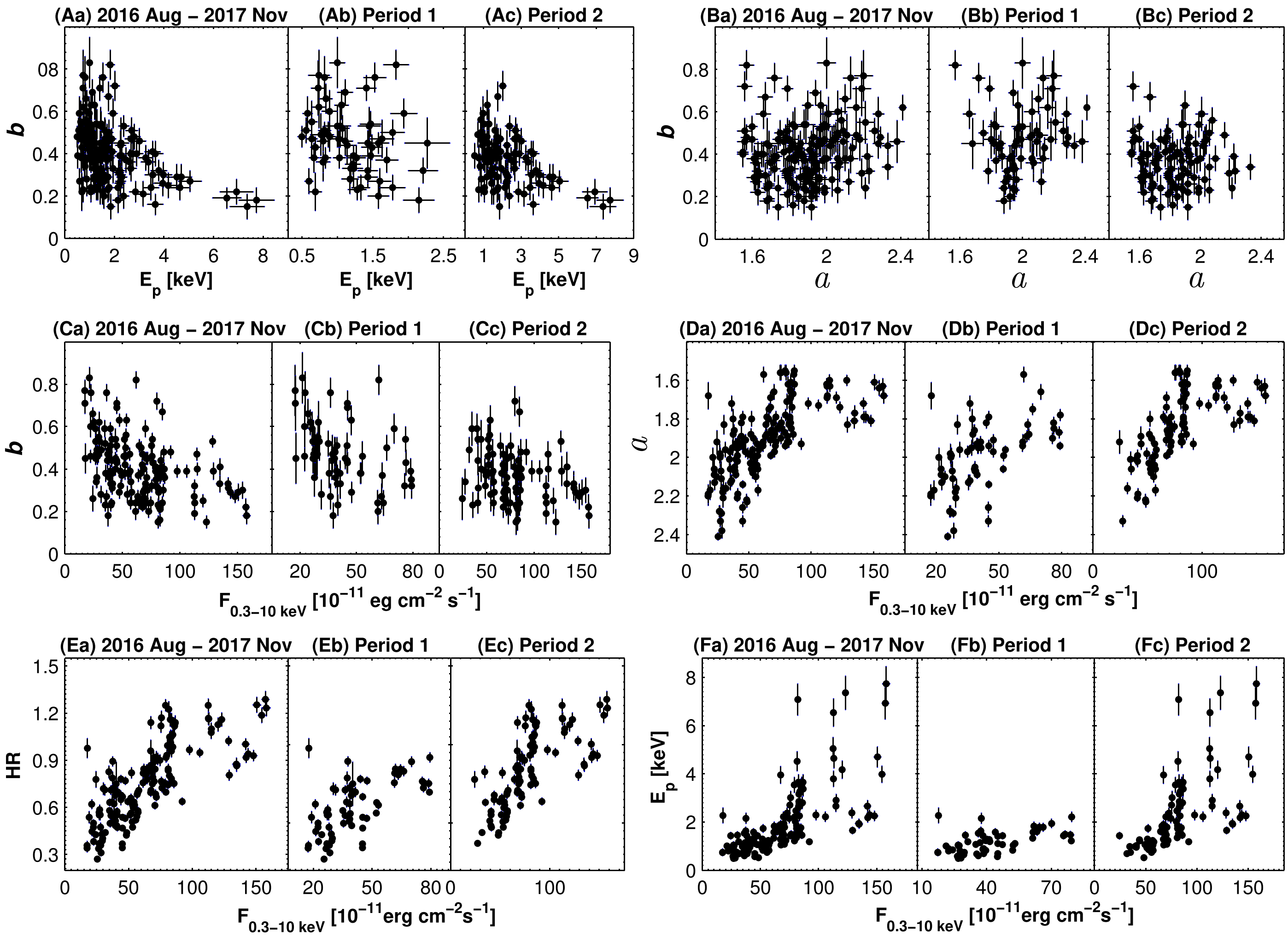

Figure 2. Correlation between the spectral parameters and fluxes.

this extreme event, the parameter $E_{\rm p}$ showed several instances of IDV by 0.50–1.60 keV (see Table 9).

4.3. Shorter-term Flares and IDV

Below, we concentrate on the detailed results of the MWL flux variability during Periods 1–2 and their different parts. The summary of the X-ray and optical–UV variability in each period and subperiod is provided in Table 8 (maximum flux, maximum-to-minimum flux ratio, and fractional variability amplitude $F_{\rm var} = 100((S^2 - \overline{\sigma^2_{\rm err}})/\overline{F})^{1/2}\%$, with S^2 the sample variance, $\overline{\sigma^2_{\rm err}}$ the mean square error, and $\overline{F}$ the mean flux (Vaughan et al. 2003).

In Period 1a, the source showed three fast 0.3–10 keV flares by a factor of ~2 that were not accompanied by any in the TeV and HE and optical–UV energy range (Figure 5(a)). The higher optical–UV states were observed in the epochs of X-ray flares, although the source showed a slower variability in this energy range. The four low-amplitude 0.3–10 keV flares by a factor of 1.7–2.4 occurred in Period 1b, which showed higher 15 GHz states along with the last two X-ray flares (Figure 5(b)). Although the LAT-band peaks were observed along with the first two 0.3–10 keV flares, the source did not show enhanced HE activity afterward. The higher optical–UV states were observed during the second and fourth X-ray flares, with some delay on the last occasion. An HE flare was observed in the epoch of the 0.3–10 keV flare by a factor of 3.2 in Period 1c, although its peak occurred a week earlier (Figure 5(c)). The optical–UV and radio light curves showed a decline during these instances.

An X-ray flare by a factor of 3.3 was accompanied by a decline and lower states in the optical–UV and HE energy ranges in Period 2a (Figure 5(d)). Similarly, the source showed an optical–UV decline along with both X-ray flares in Period 2b (Figure 5(e)). The peak of the second, stronger flare corresponded to the highest historical 0.3–10 keV state of 1ES 1959+650, which coincided with some enhancements in the HE activity, while the first, higher HE peak occurred at the beginning of this subperiod when the source was in a lower X-ray state. The source almost reached the aforementioned highest historical 0.3–10 keV brightness level on MJD 57,047 (2017 October 21, Period 2c), declining by a factor of 3.5 during the next 10 days (Figure 5(f)). We observe enhanced HE activity in the epoch of the X-ray peak, while optical–UV and 15 GHz peaks were recorded during the low X-ray states.

During 2016 August–2017 November, the source showed 32 instances of the 0.3–10 keV IDV at the 99.9% significance level. The summary of these IDVs is provided in Table 9, containing the values of reduced χ^2, fractional variability amplitude,[17] and the ranges of the spectral parameters for each instance. Figures 6

---

[17] Both count rates and de-absorbed flux values (when at least two spectra are extracted for the particular XRT observation with the 0.3–10 keV IDV) show similar values within the error ranges.

Table 7
Correlations between the Spectral Parameters and Multiband Fluxes (Denoted by "F_i" for the Particular i Band) in Different Periods

Quantities	r	p
	2016 Aug–2017 Nov	
b and $E_{\rm p}$	−0.40(0.10)	1.48×10^{-6}
a and b	0.20(0.12)	9.2×10^{-3}
b and $F_{0.3\text{–}10\,\rm keV}$	−0.39(0.10)	3.33×10^{-6}
a and $F_{0.3\text{–}10\,\rm keV}$	−0.67(0.06)	6.77×10^{-11}
HR and $F_{0.3\text{–}10\,\rm keV}$	0.69(0.05)	8.20×10^{-12}
$E_{\rm p}$ and $F_{0.3\text{–}10\,\rm keV}$	0.66(0.07)	1.66×10^{-11}
log $E_{\rm p}$ and log $S_{\rm p}$	0.74(0.08)	8.45×10^{-13}
$F_{0.3\text{–}2\,\rm keV}$ and $F_{2\text{–}10\,\rm keV}$	0.87(0.03)	$<10^{-15}$
$F_{0.3\text{–}10\,\rm keV}$ and $F_{\rm UVW2}$	−0.27(0.13)	9.18×10^{-3}
$F_{0.3\text{–}10\,\rm keV}$ and $F_{\rm V}$	−0.31(0.12)	1.27×10^{-3}
$F_{\rm UVW2}$ and $F_{\rm UVM2}$	0.94(0.01)	$<10^{-15}$
$F_{\rm B}$ and $F_{\rm V}$	0.89(0.02)	$<10^{-15}$
$F_{0.3\text{–}2\,\rm GeV}$ and $F_{2\text{–}300\,\rm keV}$	0.44(0.13)	7.50×10^{-4}
$U - V$ (mag) and U (mag)	0.34(0.11)	3.16×10^{-4}
	Period 1	
b and $F_{0.3\text{–}10\,\rm keV}$	−0.37(0.11)	9.09×10^{-6}
a and $F_{0.3\text{–}10\,\rm keV}$	−0.63(0.07)	2.31×10^{-9}
HR and $F_{0.3\text{–}10\,\rm keV}$	0.58(0.06)	6.65×10^{-8}
$E_{\rm p}$ and $F_{0.3\text{–}10\,\rm keV}$	0.50(0.07)	7.01×10^{-8}
$F_{0.3\text{–}2\,\rm keV}$ and $F_{2\text{–}10\,\rm keV}$	0.82(0.03)	$<10^{-15}$
$F_{0.3\text{–}300\,\rm GeV}$ and $F_{\rm UVW2}$	0.39(0.12)	7.20×10^{-4}
$F_{0.3\text{–}300\,\rm GeV}$ and $F_{\rm V}$	0.40(0.12)	6.11×10^{-4}
	Period 2	
b and $E_{\rm p}$	−0.38(0.11)	9.52×10^{-6}
a and $F_{0.3\text{–}10\,\rm keV}$	−0.70(0.05)	8.05×10^{-12}
a and $F_{0.3\text{–}10\,\rm keV}$	−0.51(0.11)	7.04×10^{-6}
HR and $F_{0.3\text{–}10\,\rm keV}$	0.67(0.07)	6.02×10^{-11}
$E_{\rm p}$ and $F_{0.3\text{–}10\,\rm keV}$	0.65(0.08)	3.49×10^{-10}
$F_{0.3\text{–}2\,\rm keV}$ and $F_{2\text{–}10\,\rm keV}$	0.86(0.03)	$<10^{-15}$
$F_{0.3\text{–}10\,\rm keV}$ and $F_{\rm UVW2}$	−0.33(0.12)	5.30×10^{-3}
$F_{0.3\text{–}10\,\rm keV}$ and $F_{\rm V}$	−0.40(0.11)	1.18×10^{-4}

(a) and (b) present the fastest 0.3–10 keV variability of 1ES 1959+650, incorporating brightness fluctuations by $F_{\rm var} = 5.4\%\text{–}7.5\%$ within 0.54–1.62 ks. Other IDVs occurred during those XRT observations of our target that were distributed over two or more *Swift* orbits. The two corresponding examples are provided in Figures 6(g) and (h), which were characterized by fractional amplitudes $F_{\rm var} = 4.3\%\text{–}8.9\%$. Note that the second IDV was characterized by significant spectral changes by $\Delta a = 0.18(0.05)$, $\Delta b = 0.28(0.10)$, $\Delta E_{\rm p} = 0.50(0.12)$ keV, and $\Delta{\rm HR} = 0.36(0.04)$.

Finally, Figure 7(a) presents the most densely sampled XRT observations of 1ES 1959+650 during the period 2017 June 20–27, when the brightness decreased by a factor of 2.3 ± 0.2[18] in about 3.3 days. Figures 7(b) (2016 October 30–November 5) and 7(c) (2017 November 19–24) present relatively faster brightness drops by factor of 2.1 and 2.2 instances in 1.5 days and 2.2 in 2 days, respectively. These instances were characterized by the spectral variability with $\Delta a = 0.16\text{–}0.48$, $\Delta b = 0.25\text{–}0.57$, $\Delta E_{\rm p} = 0.67\text{–}1.48$ keV, and $\Delta{\rm HR} = 0.24\text{–}0.43$. However, the source did not show flux halving or doubling during the 2017 September 19–25 campaign, and the brightness was changing by only 10%–15% in 0.85–1.32 days (Figure 7(d)).

5. Discussion and Conclusions

5.1. Particles' Acceleration and Emission Processes

During the intensive X-ray flaring activity of 1ES 1959+650 in 2016 August–2016 November, 99% of the 0.3–10 keV spectra were curved, indicating the dominance of the log-parabolic electron energy distribution in the jet emission zone, which can be established by means of specific acceleration mechanisms (see, e.g., Massaro et al. 2004, 2011a). Namely, the most commonly considered mechanism is the stochastic acceleration arising from magnetic turbulence close to a shock front, being at work in combination with the systematic acceleration (arising during the jet launching and collimation), as well as with radiative and adiabatic cooling (Tramacere et al. 2009). The simulations of Virtanen & Vainio (2005) demonstrated that the particles's energy spectrum may undergo a gradual shift to higher energies as particles are accelerated stochastically behind the relativistic shock front. However, a relatively low spectral curvature ($b \sim 0.3$) is predicted in the case of efficient stochastic acceleration in jets of TeV-detected BL Lacs (see Massaro et al. 2011a). Our spectral analysis showed that our target mostly showed significantly larger curvature ($b \sim 0.5$ and higher) in Period 1, and an anticorrelation b–$E_{\rm p}$, also expected in the case of efficient stochastic acceleration, was not observed for these spectra. Therefore, we suggest that the stochastic acceleration was less efficient for our target in this Period 1. Note that Massaro et al. (2011b) predicted a low probability (∼12%) for the generation of TeV photons in HBL sources when the curvature is larger than the boundary value $b_* = 0.55$. In fact, the FACT observations did not show the detections of the source with 3σ significance along with those XRT observations of the 1ES 1959+650 yielding the spectra with $b > b_*$. In contrast, this anticorrelation was observed in Period 2, which also showed, on average, a lower mean value of the parameter b. Therefore, we conclude that the X-ray-emitting electrons should undergo a more efficient stochastic acceleration during the flares observed in Periods 2 than those in Period 1.

Moreover, our spectral data set from Period 2 showed the relation between the position of the synchrotron SED peak and the corresponding flux $S_{\rm p}$ as follows: $S_{\rm p} \propto E_{\rm p}^{\alpha}$ with $\alpha = 0.63 \pm 0.06$ (Figure 8(c)), which is close to the case $\alpha = 0.6$: a transition from the Kraichnan spectrum of the turbulence with the exponent $q = 3/2$ into the "hard-sphere" spectrum ($q = 2$). The simulations of Tramacere et al. (2011) show that the momentum-diffusion coefficient $D_{\rm p}$ also is variable during the stochastic acceleration of the particles for the case $\alpha = 0.6$, yielding the change in the particle's acceleration timescale as $t_{\rm acc} \sim D_{\rm p}^{-1}$. The same simulations showed a possibility of the anticorrelation b–$E_{\rm p}$ during the variability of the parameters q and $D_{\rm p}$ that was observed in Period 2 (see Section 3.2). In Period 1, $\alpha = 0.43 \pm 0.06$ (Figure 8(b)), which is beyond the range $\alpha = 0.6\text{–}4.0$ (when the observed spectral variability is driven by the particular physical process: change in the turbulence spectrum, number and energy of emitting particles, magnetic field, and Doppler factor; see Tramacere et al. 2011, for details). This result leads us to the conclusion that the observed spectral variations in this

---

[18] A similar value of the brightness decline factor is derived using the corresponding de-absorbed 0.3–10 keV fluxes.

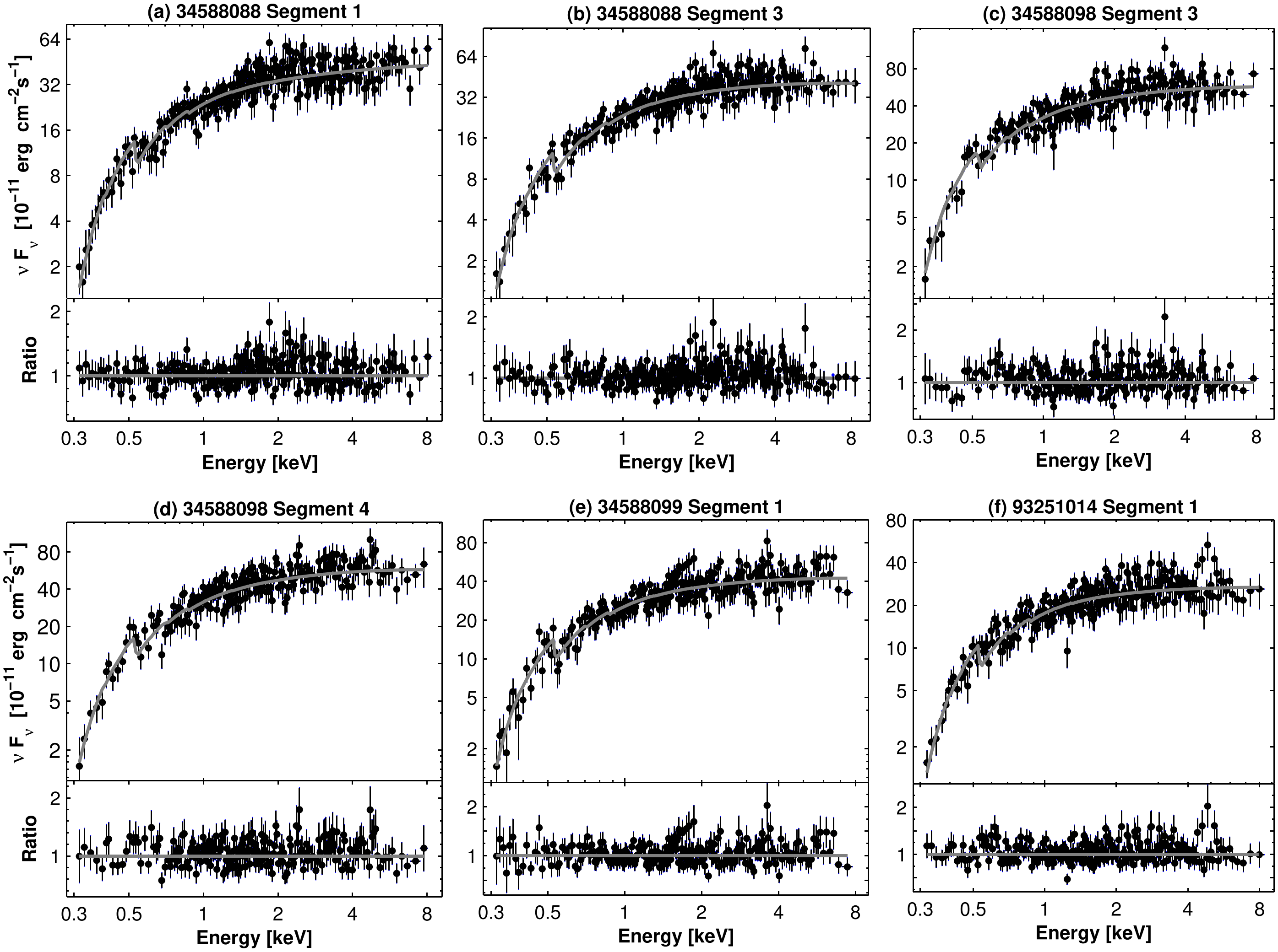

Figure 3. The 0.3–10 keV spectra with $E_{\mathrm{p}} > 5$ keV, along with the distribution of the residuals.

period were triggered by the underlying complex physical conditions, with no dominant factor.

A log-parabolic electron energy distribution can also be established by the energy-dependent acceleration probability process (EDAP), which is based on the first-order Fermi mechanism operating at the shock front in the magnetized jet medium, where the confinement efficiency of relativistic electrons by a magnetic field decreases with increasing gyroradius (see Massaro et al. 2004, for details). In that case, we should observe a positive *a*–*b* correlation. Although our target also showed this correlation in the period presented here, it was very weak, probably due to the "competition" with the other types of acceleration mechanisms, e.g., stochastic acceleration, which does not yield the *a*–*b* correlation. According to the simulations of Katarzynski et al. (2006), a charged particle can be accelerated at the shock front by the first-order Fermi process and then continue gaining an additional energy via the stochastic mechanism in the shock downstream region. Eventually, the particle will be able to reenter the shock acceleration region and repeat the combined acceleration cycle. In this case, a positive *a*–*b* correlation will be weak and may not even be observed.

Note that 18% of all log-parabolic spectra were harder than $a = 1.70$, which rarely have been observed in HBLs (without significant contribution from the photons of the IC origin in the 0.3–10 keV energy range, yielding a flattening or even upward curvature of X-ray spectra). Moreover, our target often exhibited very hard HE spectra with the 0.3–300 GeV photon index $\Gamma < 1.70$ during 2016 August–2017 November (see Table 10). According to Shukla et al. (2015), the origin of such spectra can be explained much more easily in the framework of hadronic scenarios, while achieving a hard γ-ray spectrum from leptonic models is more challenging. For example, the proton blazar model, introduced by Mannheim (1992), predicts the generation of HE spectra with the photon index $\Gamma < 2$. Moreover, below a few MeV, the spectrum should flatten to an X-ray spectrum with the index of 1.5–1.7 (observed in the target during strong X-ray flares). Furthermore, an uncorrelated X-ray–TeV variability (frequently observed for our target) can be explained more easily by hadronic scenarios.

Moreover, we extracted the 0.3–2 and 2–300 GeV photon fluxes to examine their cross-correlation in the period presented here. This study may allow us to draw a conclusion about the possible contribution of the different particle population to the observed HE emission. We used 2-week binned observations of 1ES 1959+650 to ensure that the number of the predicted photons N_{pred} equals at least 10 (especially in the 2–300 GeV energy range; otherwise, the derived photon fluxes and

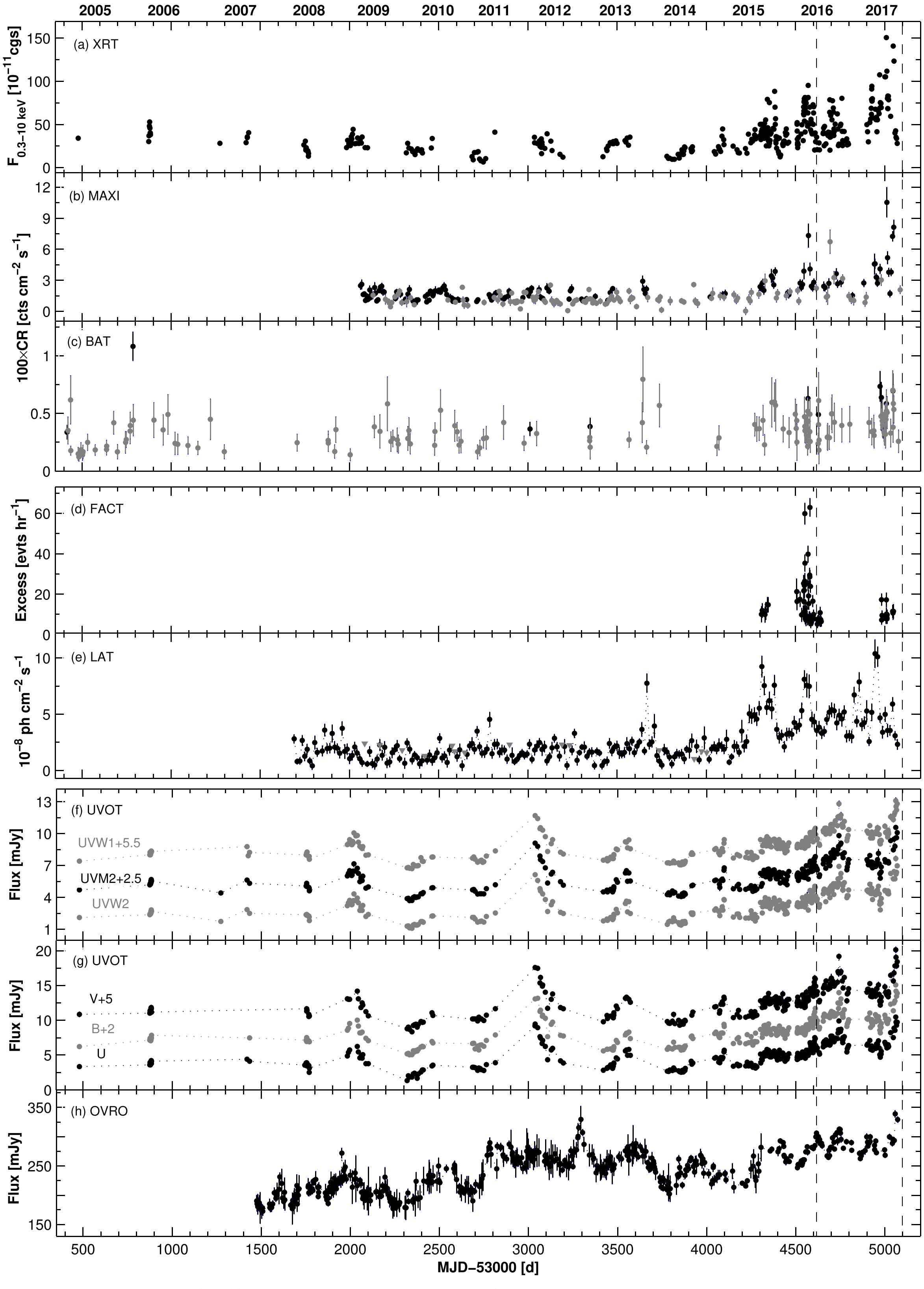

Figure 4. Historical light curves of 1ES 1959+650 from the MWL observations in 2005–2017 with XRT (top panel), *MAXI* (panel (b)), *BAT* (panel (c)), FACT (panel (d)), LAT (panel (e)), UVOT (panels (f) and (g)), and OVRO and MOJAVE (panel (j)). We used daily bins for the XRT, BAT, FACT, UVOT, Steward, OVRO, and MOJAVE data, and 1- and 2-week bins for those of *MAXI* and LAT, respectively. In panel (a), the acronym "cgs" denotes erg cm^{-2} s^{-1}. In panels (b) and (c), black and gray points stand for the detections with 5σ and 3σ significances, respectively. Gray triangles in panel (e) represent 2σ upper limits to the LAT flux when the source was detected below the 3σ significance. The 2016 August–2017 November period is indicated by vertical dashed lines.

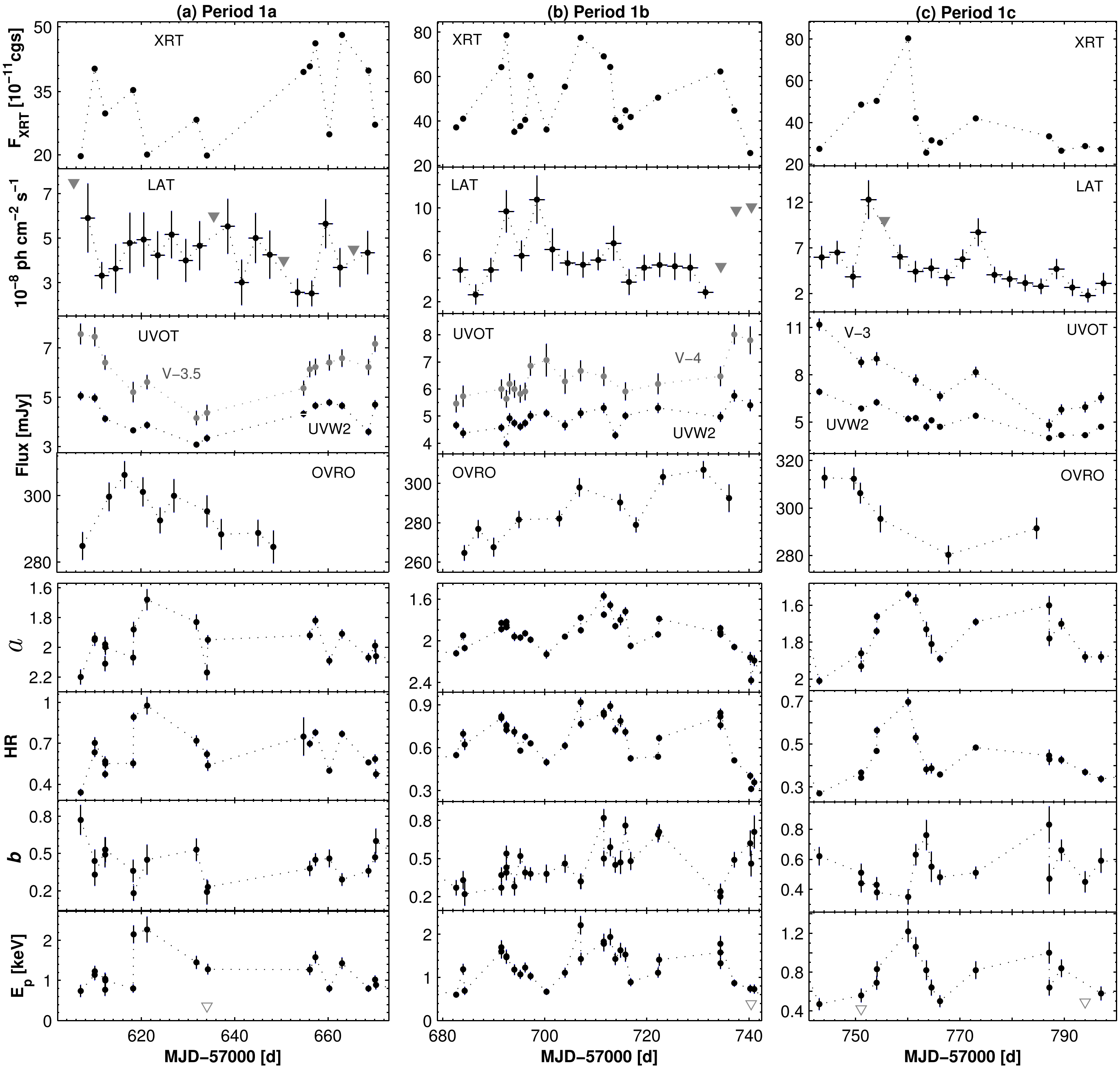

Figure 5. Variability of the MWL flux and spectral parameters in different subperiods. Gray triangles in LAT-band panels stand for upper limits to the LAT flux when the source was detected below 3σ significance. In the top panels, the acronym "cgs" denotes erg $\mathrm{cm}^{-2}\ \mathrm{s}^{-1}$. The triangles in the bottom panels denote upper limits to the parameter E_{p} (see the next page for Figures 8(d)–(f)).

corresponding indices could be less credible; see Table 10). Figure 9(a) and Table 7 demonstrate that the $F_{0.3\text{–}2\ \mathrm{GeV}}$–$F_{2-300\ \mathrm{GeV}}$ correlation was weak during 2016 August–2017 November, hinting at the uncorrelated behavior and possible contribution from different particle populations in some time intervals (see also Figures 9(c) and (e)). The indices $\Gamma_{0.3\text{–}2\ \mathrm{GeV}}$ and $\Gamma_{2\text{–}300\ \mathrm{GeV}}$ also show a weak cross-correlation (Figures 9(a), (c), and (d)). In five cases, the index $\Gamma_{2\text{–}300\ \mathrm{GeV}}$ was harder than its lower-energy "counterpart" that could be related to the hadronic contribution to the HE emission of 1ES 1959+650 (see the data points in the upper left part of Figure 9(b) and the corresponding results in Table 10).

On the contrary, Figure 9(b) also shows the data points corresponding to a harder 0.3–2 GeV spectrum compared to the higher-energy one (those situated right below the dashed line in the $\Gamma_{0.3\text{–}2\ \mathrm{GeV}} = \Gamma_{2\text{–}300\ \mathrm{GeV}}$ plane; see also Table 10). These occasions can be related to the upscatter of X-ray photons in the 2–300 GeV energy range in the Klein-Nishina (K-N) regime, yielding a steepening of the corresponding photon spectrum with respect to that established in the 0.3–2 GeV range by means of the Thompson upscattering of the optical–UV photons. Alternatively, Patel et al. (2018) suggested the existence of different emission regions for lower- and higher-energy photons in the LAT band (0.1–3 GeV and 3–300 GeV bands, respectively) in the period 2014 December–2017 February since these emissions exhibited different spectral trends in the photon index–flux plane. They supposed that there should be a different emission region of optical/UV photons

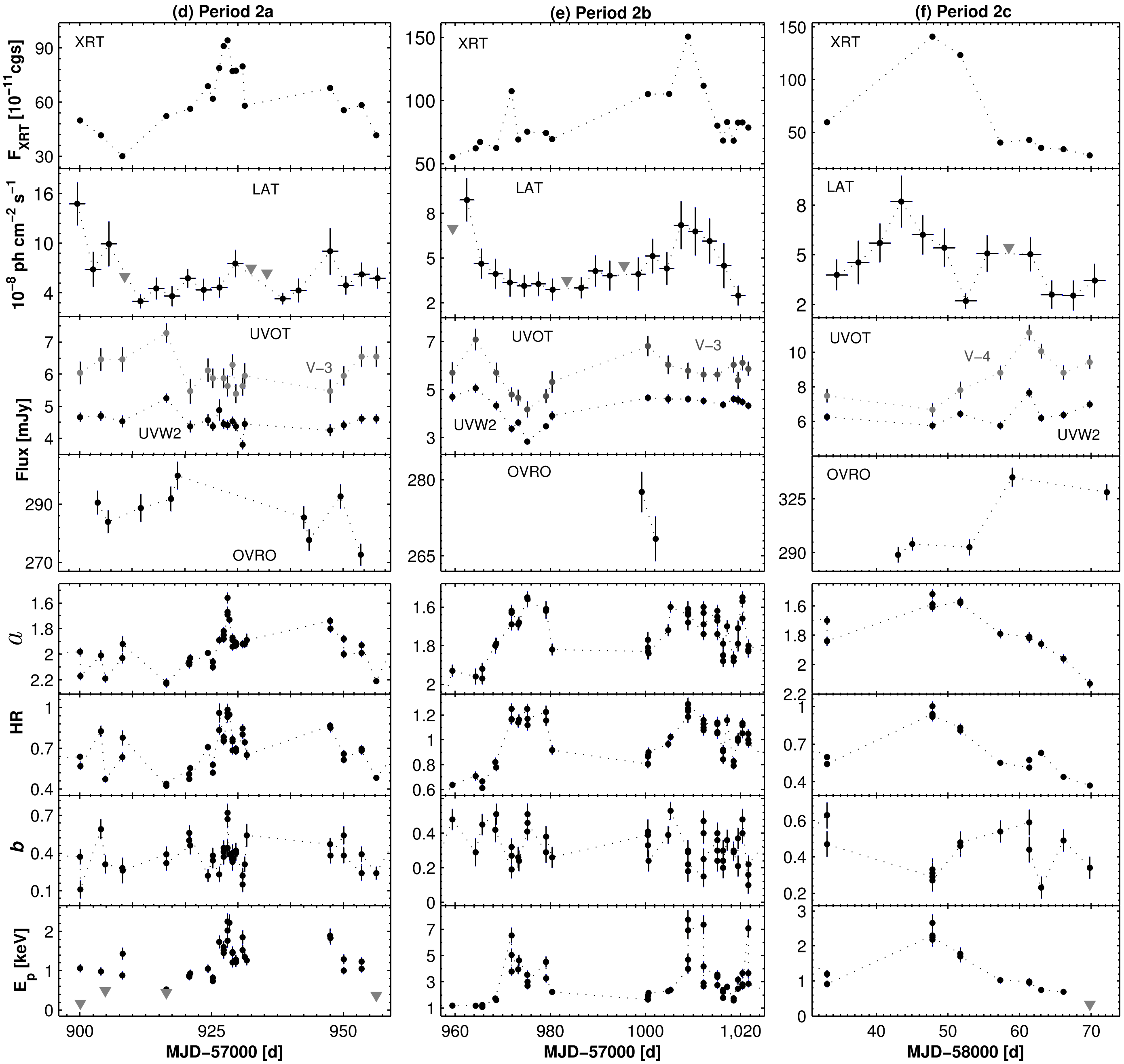

Figure 5. (Continued.)

and that these photons are upscattered to low-energy γ-rays (see, however, our discussion in Section 5.2.2).

5.2. Flux Variability and Interband Correlations

5.2.1. X-Rays

During the 1.25 yr period presented here, 1ES 1959+650 continued its trend of progressively higher X-ray flaring activity shown since 2015 August, possibly owing to the long-term increase in the collimation of high-energy plasma through the jet. A general higher state (compared to previous years, which may be the result of the increasing amount of the high-energy plasma transported through the jet) was superimposed by low-amplitude or stronger flares by a factor of 1.7–3.5, especially in Period 2, when the source attained its new highest historical 0.3–10 keV twice and became the second BL Lac source (after Mrk 421) exceeding a level of 30 counts s^{-1} (corresponding to about 1.3×10^{-9} erg cm^{-2} s^{-1}). Note that 1ES 1959+650 was the brightest blazar in the 0.3–10 keV energy during 2017 June 23–26, exceeding that of Mrk 421 (generally, the brightest blazar in X-rays) during that time interval (see Table 1). The same could occur during the period 2017 September-October, but there were no XRT observations of Mrk 421 in that period owing to the Sun angle restriction.

Moreover, Period 2 is notable also for another fact: the source exceeded the previous highest de-absorbed 0.3–10 keV flux of $(1.04 \pm 0.02) \times 10^{-9}$ erg cm^{-2} s^{-1} recorded on 2016 July 2 (MJD 57,571) 20 times and attained the value $(1.57 \pm 0.03) \times 10^{-9}$ erg cm^{-2} s^{-1}. Among bright HBLs,

Table 8

Summary of the XRT and UVOT Observations in Different Periods

	XRT								UVOT											
Per. (1)	$\mathrm{CR}_{\max}$ (2)	R (3)	$F_{2-10}^{\max}$ (4)	$R_{2\text{–}10}$ (5)	F_{var} (6)	$F_{0.3-2}^{\max}$ (7)	$R_{0.3\text{–}2}$ (8)	F_{var} (9)	R_{W2} (10)	F_{var} (11)	R_{M2} (12)	F_{var} (13)	R_{W1} (14)	F_{var} (15)	R_{U} (16)	F_{var} (17)	R_{B} (18)	F_{var} (19)	R_{V} (20)	F_{var} (21)
1	20.86	4.0	3.80	8.6	54.4(0.5)	4.68	5.2	34.5(0.3)	2.2	14.7(0.5)	2.1	14.7(0.4)	2.2	14.0(0.6)	1.9	12.4(0.5)	1.8	11.5(0.4)	1.9	11.5(0.6)
1a	12.42	2.3	3.66	5.0	29.9(0.5)	2.68	3.0	25.7(0.6)	1.6	15.1(1.0)	1.5	13.1(0.8)	1.5	10.5(1.1)	1.5	10.8(0.9)	1.5	10.1(0.7)	1.4	10.2(1.0)
1b	20.43	3.9	7.94	4.5	34.4(0.4)	4.51	3.5	28.5(0.4)	1.4	8.0(0.8)	1.4	8.5(0.7)	1.4	4.6(0.8)	1.3	7.6(0.8)	1.3	5.5(0.7)	1.3	5.7(1.0)
1c	20.86	3.2	7.93	3.7	41.4(0.5)	4.68	3.2	34.1(0.5)	1.7	16.4(1.0)	1.8	18.6(0.8)	1.9	17.1(1.2)	1.8	16.5(0.9)	1.7	16.5(0.7)	1.8	17.8(1.1)
2	39.18	5.4	10.30	13.9	53.0(0.4)	12.39	9.0	39.8(0.2)	2.7	19.6(0.6)	2.4	21.0(0.5)	2.2	17.2(0.7)	2.2	19.5(0.5)	2.2	18.6(0.4)	2.1	18.2(0.6)
2a	24.50	3.2	5.15	4.8	37.4(0.6)	5.62	4.1	23.4(0.3)	1.4	5.2(1.0)	1.3	5.1(0.8)	1.3	4.5(1.1)	1.3	4.8(0.8)	1.3	6.8(0.7)	1.2	4.1(1.1)
2b	39.18	2.7	8.85	3.8	33.5(0.8)	7.23	2.5	26.0(0.3)	1.8	13.5(0.9)	1.7	13.1(1.0)	1.5	9.8(1.1)	1.5	11.1(0.9)	1.5	8.9(0.7)	1.4	7.6(1.1)
2c	36.63	5.0	10.30	13.9	83.6(1.1)	12.39	6.2	68.6(0.1)	1.3	9.3(1.2)	1.4	9.2(0.9)	1.3	9.3(1.8)	1.4	10.0(1.1)	1.4	10.8(0.9)	1.4	10.9(1.2)

Note. Columns (2)–(4): maximum 0.3–10 keV flux (in counts s^{-1}), maximum-to-minimum flux ratio, and fractional amplitude (in percent), respectively. Maximum de-absorbed flux (in 10^{-10} erg cm^{-2} s^{-1}), maximum-to-minimum flux ratio, and fractional amplitude in 2–10 keV (Cols. (5)–(6)) and 0.3–2 keV (Cols. (7)–(8)) bands. Columns (10)–(21): maximum-to-minimum flux ratio and fractional amplitude in the UVOT bands.

Table 9
Summary of the 0.3–10 keV IDVs in 2017 August–2017 November

ObsID(s)/Date (1)	ΔT (hr) (2)	χ^2/dof (3)	Bin (4)	$F_{\rm var}$ (%) (5)	*a* (6)	*b* (7)	$E_{\rm p}$ (keV) (8)	HR (9)
34588023/2016 Aug 06	13.57	152.6/1	Or	17.4(1.0)	1.88(0.05)–2.07(0.05)	0.18(0.06)–0.36(0.09)	0.80(0.10)–2.15(0.22)	0.55(0.03)–0.89(0.03)
34588025/2016 Aug 31	0.28	2.51/16	60 s	7.5(1.7)	1.83(0.05)	0.53(0.09)	1.45(0.16)	0.72(0.04)
34588026/2016 Sep 03	2.66	25.55/1	Or	8.9(1.3)	2.17(0.04)	0.19(0.10)	0.36(0.08)	0.54(0.04)
34588032/2016 Sep 29	0.28	2.78/16	60 s	6.9(1.5)	2.09(0.03)	0.46(0.07)	0.80(0.09)	0.50(0.02)

Note. Column (3) gives the total observation duration (including the intervals between the orbits). In Column (1), the abbreviation “or” denotes “orbit.”

(This table is available in its entirety in machine-readable form.)

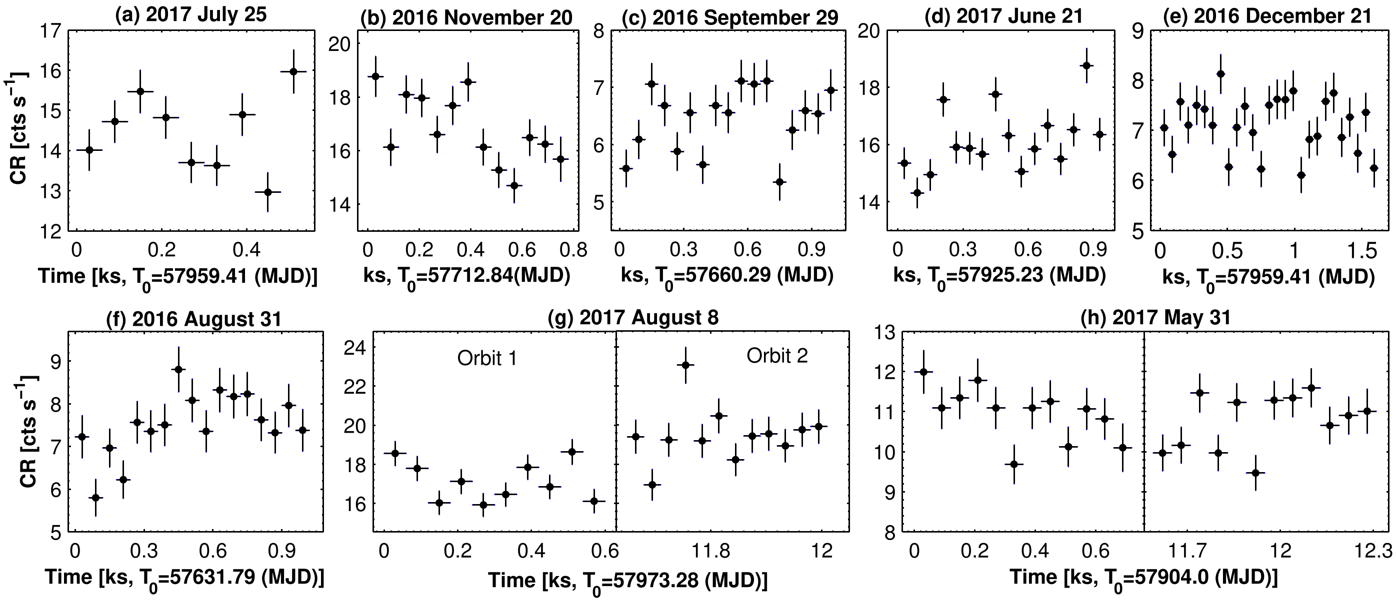

Figure 6. Most notable X-ray IDVs of 1ES 1959+650 in 2016 August–2017 November.

Mk 421 is the only other source showing the 0.3–10 keV flux above the level of 10^{-9} erg cm^{-2} s^{-1} (see, e.g., Kapanadze et al. 2018a, 2018c). The mean 2–10 keV flux from the period 2016 August–2017 November was 31% higher than that from the XRT observations performed in 2016 February–July. We continue the intensive ToO campaign of the extended X-ray flaring activity of our target with the XRT (along with the simultaneous optical–UV and VHE observations with the UVOT and FACT telescopes, respectively).

During 2016 August–2017 November, our target was active on intraday timescales, and the corresponding duty cycle (DC, i.e., the fraction of total observation time during which the object displays a variability) amounted to 40% ± 2%, which is higher than that corresponding to the IDVs in 2005–2014 and 2015 August–2016 January (DC < 30%). On the other hand, the source was more active on intraday timescales during 2016 February–July (52% ± 2%; Kapanadze et al. 2018a), and these instances mostly were observed during higher X-ray states, similarly to the period presented here (Figure 10(a)). Note that this result is favored by the “shock-in-jet” scenario (see, e.g., Sokolov et al. 2004, and references therein), where an IDV is triggered by the interaction of a propagating shock front with jet inhomogeneities. Moreover, the source showed very fast 0.3–10 keV IDVs occurring within 1 ks exposures, which could be related to the smallest-size jet turbulent structures, producing a very rapidly variable emission due to the light-travel argument. According to the relativistic magnetohydrodynamic simulations of Mizuno et al. (2014), such structures may have the strongest magnetic fields in the jet and can produce higher-energy photons, including those corresponding to the 0.3–10 keV energy range. These simulations also demonstrated that a shock propagation can strongly amplify the turbulence in the shocked jet material, and more frequent detection of the 0.3–10 keV IDVs in the period presented here than during 2005–2014 and 2015 August–2016 January was possibly due to more strongly developed turbulence in this period. On the contrary, the majority of the 0.3–10 keV IDVs in the later periods were observed in lower X-ray states of the source, and these instances may be triggered by an instability occurring in the innermost AGN area: such IDVs should be more conspicuous in low brightness states when the variable emission from the innermost AGN area will not be “shadowed” by that produced at the front of the shock front that is propagating through the jet.

On the other hand, the source showed an extreme drop of X-ray brightness by a factor of 2.7 ± 0.2 in about 18 hr in the period 2015 August–2016 January, and a more extreme drop by a factor of 2.3 ± 0.2 in 4.8 hr that occurred in 2016 February–July (Kapanadze et al. 2016a, 2018a), while the flux-doubling/halving instances were not observed on intraday timescales in the period presented here: the source showed the flux-halving times $\tau_{\rm h} = 1.3$–2.7 days during the densely sampled XRT observations. Such extreme brightness drops can be related to the transition of the relativistic shock front from the area with highly developed turbulence (and having stronger magnetic field) into that with lower turbulence and weaker magnetic field, yielding the generation of significantly fewer X-ray photons. The XRT observations of 1ES 1959+650 have not shown any flux-doubling instance on intraday timescales, although it occurred in the 3–79 keV energy range during the 30 ks exposure with *NuSTAR* on 2014 September 17 (Pandey et al. 2017). This result (along with the higher values of $F_{\rm var}$ in the 2–10 keV band than in the 0.3–2 keV one in different epochs; see below) implies that the electron energy distribution in our target generally is characterized by a peak at the energies necessary to produce hard X-ray photons and yielding a weaker variability in the soft X-ray energy range.

On the other hand, 1ES 1959+650 was passive on intraday timescales during some densely sampled XRT observations in 2016 August–2017 November: we have found the 81 ks time interval during which the source did not vary at the 99.9% confidence level, or a very slow variability by less than 30% during the interval as long as 3 days was also observed. This result may hint at weakly developed turbulence (yielding a less efficient stochastic acceleration) in the X-ray emission zone of our target during some time intervals of the period presented here, which, in turn, was reflected in the weakness of the expected b–$E_{\rm p}$ anticorrelation.

The de-absorbed, soft 0.3–2 keV and hard 2–10 keV fluxes showed a positive cross-correlation during 2016 August–2017

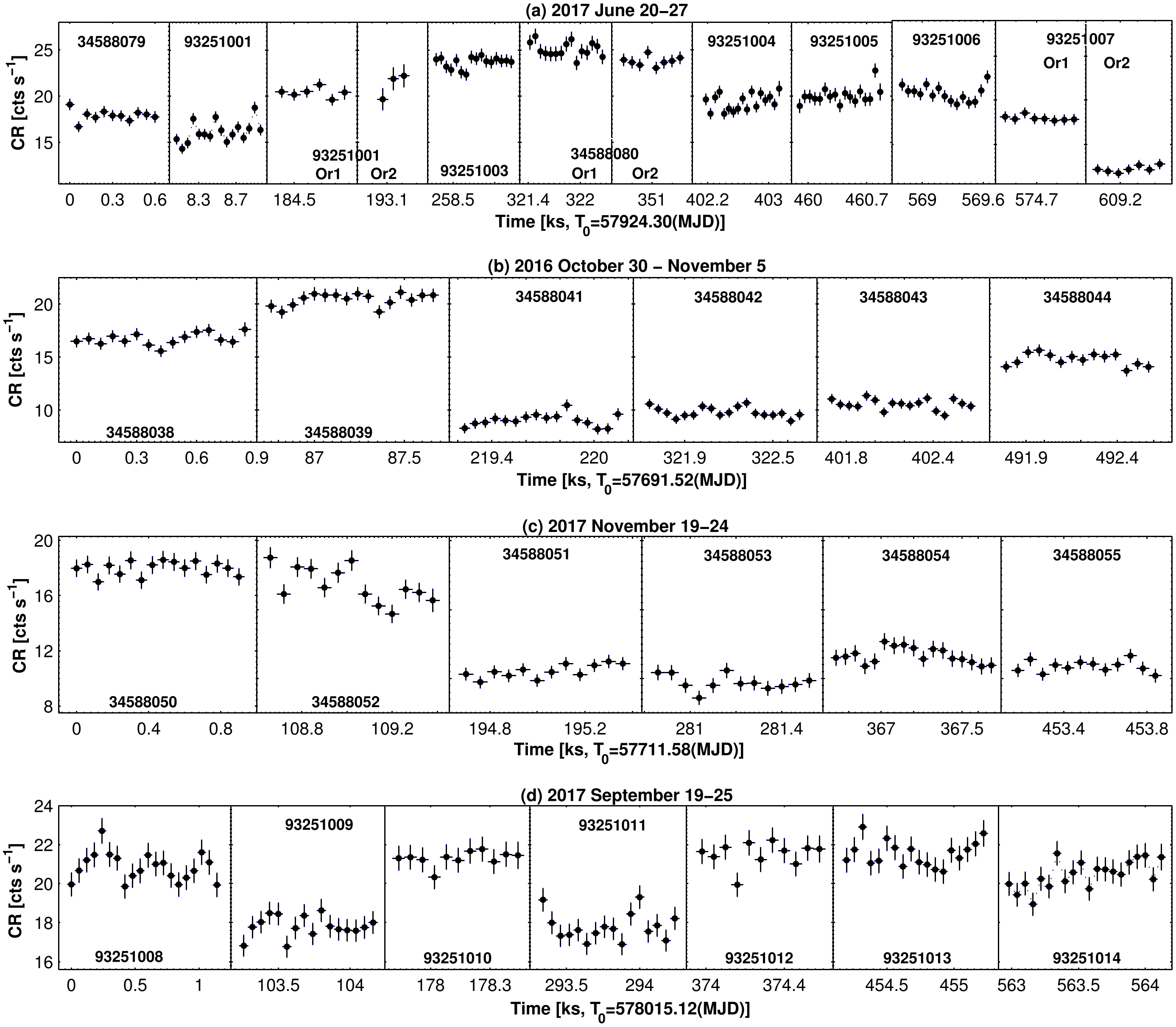

Figure 7. The 0.3–10 keV light curves from the most densely sampled XRT observations of 1ES 1959+650 during 2017 August–2018 November.

Table 10

Results from 2-week Binned LAT Data in the 0.3–2 GeV and 2–300 GeV Energy Ranges during 2016 August–2017 November

	0.3–2 GeV				2–300 GeV			
Dates (1)	TS (2)	N_{pred} (3)	Flux (4)	Γ (5)	TS (6)	N_{pred} (7)	Flux (8)	Γ (9)
2016 Aug 06–20	42.3	33.8	2.81(0.62)	1.65(0.20)	82.8	12.81	0.86(0.17)	1.72(0.12)
2016 Aug 20–Sep 03	43.4	38.8	2.41(0.53)	1.39(0.20)	118.9	17.2	0.87(0.09)	2.17(0.11)
2016 Sep 03–17	71.2	51.4	3.32(0.69)	1.98(0.18)	82.0	13.6	0.69(0.13)	2.07(0.12)
2016 Sep 17–Oct 01	51.7	27.1	1.92(0.35)	1.31(0.20)	158.6	18.1	1.09(0.14)	1.67(0.09)

Note. Columns (2) and (6): test statistics corresponding to 1ES 1959+650 in each band. Columns (3) and (7): number of the model-predicted photons. Photon fluxes (Columns (4) and (8)) are provided in units of 10^{-8} photons cm^{-2} s^{-1}.

(This table is available in its entirety in machine-readable form.)

November (see Table 7 and Figure 11(A)), although the hard flux often varied by a larger amplitude (see the bottom panels of Figures 12(a)–(f), as well as Table 8 for the value of f_{var} and maximum-to-minimum flux ratio R for each band in different subperiods). The difference in the variability strength was the largest in Period 2c when the 0.3–2 keV flux varied with $R = 6.2$, while this ratio amounted to 13.9 in the 2–10 keV band. The difference between the variability strength in the

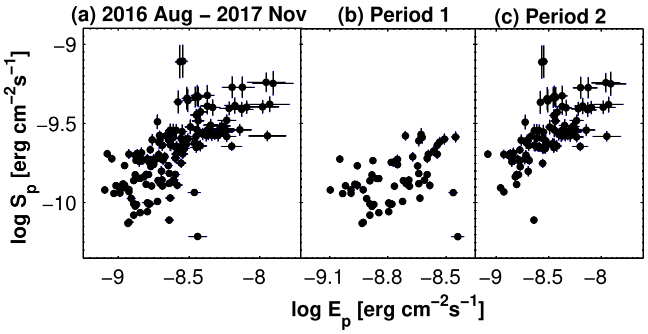

Figure 8. S_p–E_p relation in different periods.

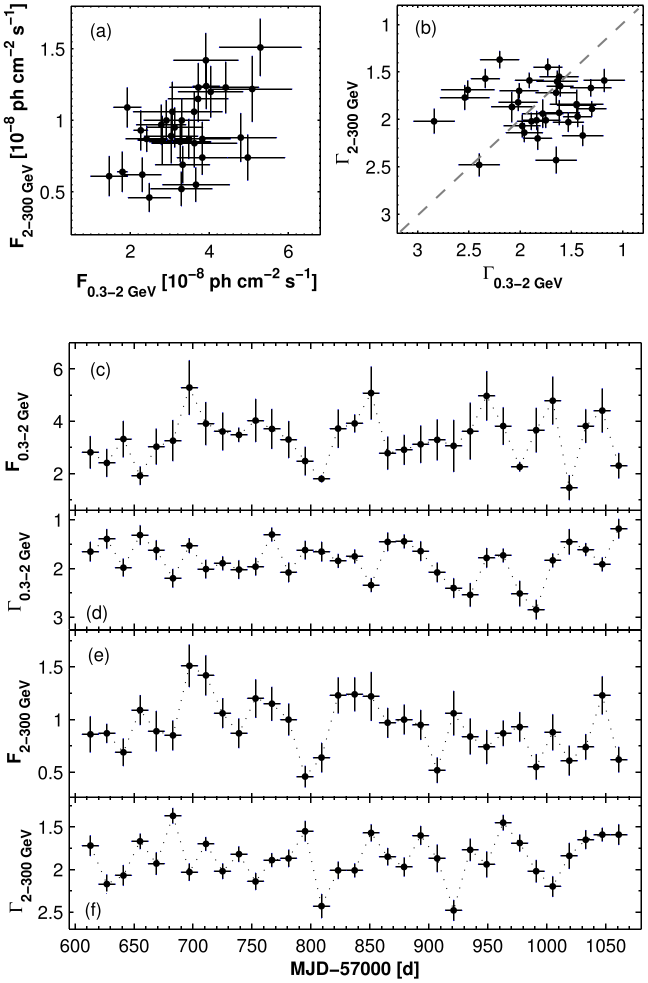

Figure 9. The 0.3–2 GeV and 2–300 GeV fluxes and photon indices of 1ES 1959+650 in 2016 August–2017 November. The 0.3–2 GeV and 2–300 GeV fluxes (panels (a), (c), and (e)) are given in units of 10^{-8} photons cm^{-2} s^{-1}. In panel (b), the dashed line corresponds to the case $\Gamma_{0.3\text{–}2\ \text{GeV}} = \Gamma_{2\text{–}300\ \text{GeV}}$.

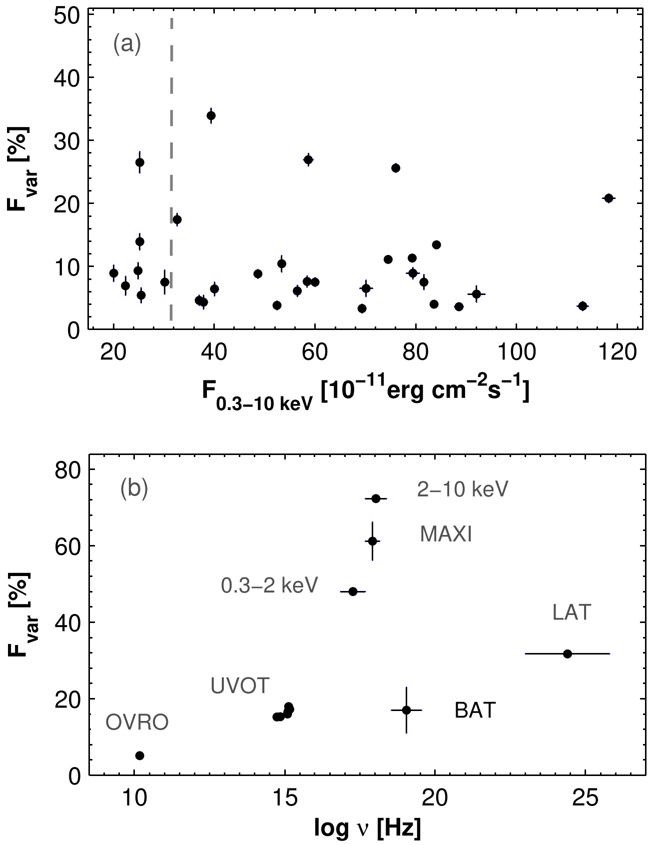

Figure 10. (a) Fractional variability amplitude of the X-ray IDVs as a function of the XRT-band flux in 2016 August–2017 November. A vertical dashed line stands for the mean 0.3–10 keV flux during 2005–2017. (b) Fractional variability amplitude as a function of frequency in the same period.

0.3–2 keV and 2–10 keV bands was evident also during some X-ray IDVs discussed in Section 4.3 that led to some scatter of the data points in Figure 11(A), constructed using the simultaneous hard and soft flux values, and weakened the observed correlation.

The difference in the variability at the soft and hard X-ray frequencies resulted in a loop-like spectral evolution in the HR–flux plane during X-ray flares (so-called spectral hysteresis; Figure 12). Namely, our target followed clockwise (CW) loops during some low-amplitude or strong X-ray flares in Periods 1a–1c and 2a–2c (see Figures 12(a)–(f) and Table 11). Note that such a spectral evolution has an important physical implication: the acceleration and synchrotron cooling timescales of the X-ray-emitting particles and flux variability timescale (denoted as τ_{acc}, τ_{syn}, and τ_{var}, respectively) can be related as $\tau_{\text{syn}} \gg \tau_{\text{var}} \gg \tau_{\text{acc}}$, or $\tau_{\text{syn}} \gg \tau_{\text{acc}} \gg \tau_{\text{var}}$ (Kirk & Mastichiadis 1999). In that case, the spectral evolution of the source is driven by the flaring component emerging in the hard X-ray band (triggered by a rapid injection of very energetic particles in the emission zone), making the spectrum progressively harder in the brightening phase of the source and softer during the declining one. Consequently, the flux variability in the hard X-ray range leads that of the soft X-rays during the flaring and declining phases, and a so-called soft lag can be observed (Falcone et al. 2004). For example, the source showed possible soft lags at MJD 57,610 and 57,663 (see the bottom panel of Figure 12(a)), MJD 57,695 (Figures 12(b)), etc. (although short XRT observations with much longer intervals between them do not allow us to drive the values of the soft delay τ_{soft} by means of the commonly used technique). Note that the source showed a CW-type evolution during the 0.3–10 keV IDV observed on 2017 June 24 (MJD 57928; Figure 7(a)), while no clearly expressed spectral loops were observed on intraday timescales during past years.

Note that the relation $\tau_{\text{syn}} \gg \tau_{\text{acc}} \gg \tau_{\text{var}}$ is not applicable for those cases that show symmetric or nearly symmetric flare

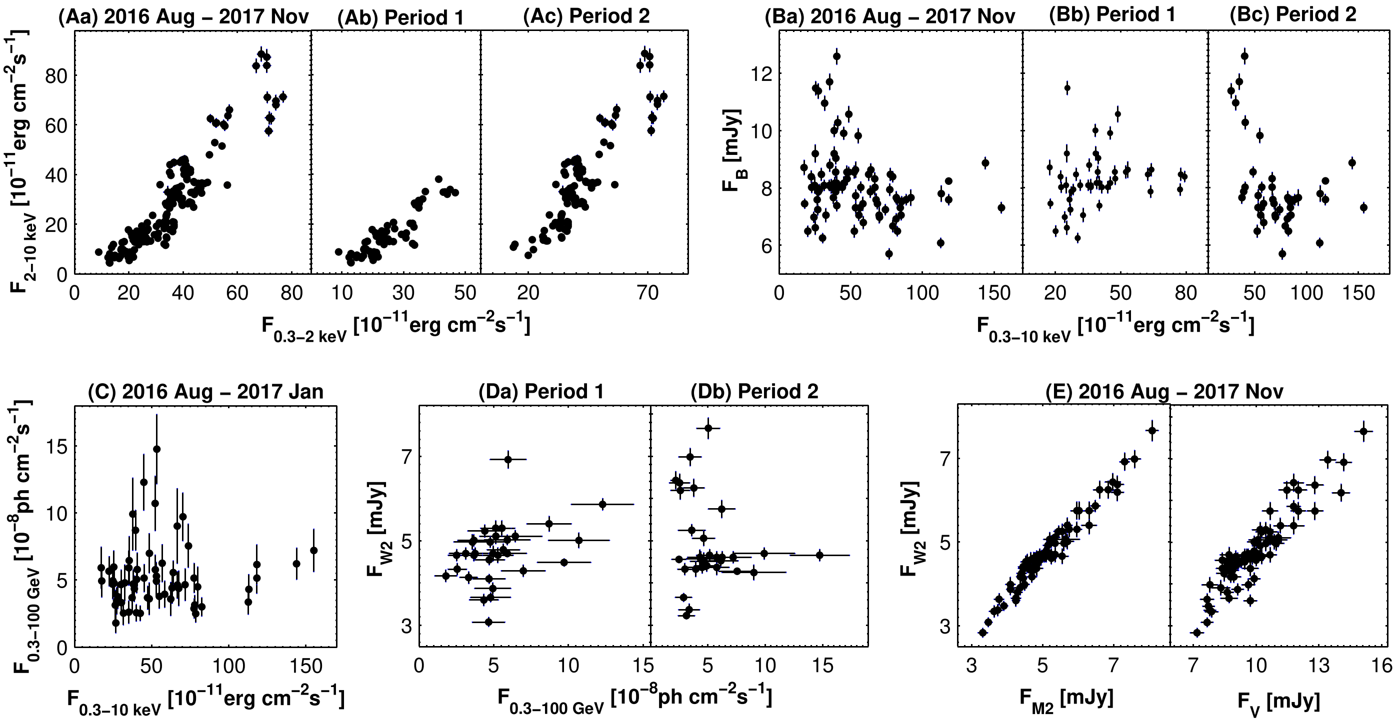

Figure 11. Correlations between multiband fluxes.

profiles (Cui 2004). Such a profile was observed for the 0.3–10 keV flare in the beginning of Period 1a (Figure 5(a)), and therefore the aforementioned timescales should have an interplay $\tau_{\rm syn} \gg \tau_{\rm var} \gg \tau_{\rm acc}$ for this flaring instance.

The source showed a counterclockwise (CCW) evolution during some flares in Periods 1a–1c and 2a–2b (see Figures 12(a)–(e) and Table 11). During the CCW-type spectral evolution, the particle's acceleration and synchrotron cooling, as well as flux variability timescales, show the interplay $\tau_{\rm syn} \approx \tau_{\rm acc} \approx \tau_{\rm var}$ (Cui 2004). As a result, the particles are gradually accelerated, with the flare at soft X-rays leading that at higher energies, and the brightness decline epoch can be dominated by the particle escape effects. Consequently, a hard lag during the X-ray flare is expected. The corresponding 0.3–2 keV and 2–10 keV light curves show possible hard lags at MJD 57,656 (Figure 12(a)), MD 57,713 (Figure 12(a)), MJD 57,927 (Figure 12(d)), etc. Note that the period 2015 August–2016 March was clearly dominated by the CCW-type spectral evolution (see Kapanadze et al. 2018a), which was not the case in the period presented here. Moreover, the source showed a transition from a CW-type loop into the opposite one during some flaring instances and vice versa. This result leads us to the suggestion that those apparently single flares could be a superposition of two or more flaring components with different particle injection/acceleration history. This possibility can also be related to the fact that the source did not show clear CW or CCW loops during some intervals of the presented period. Such intervals sometimes showed the cases when the source did not undergo a spectral variability with the brightness increase or decline. This behavior is expected for the source when the acceleration and synchrotron cooling timescales of electrons and the flux variability timescale are related as $\tau_{\rm var} \gg \tau_{\rm sync} \gg \tau_{\rm acc}$ (Cui 2004).

5.2.2. X-Rays versus VHE and Optical–UV Emissions

Similarly to the past years when the source underwent "orphan" TeV flares in 2002 June (Krawczynski et al. 2004), 2009 May, and 2012 May (Kapanadze et al. 2016b), or X-ray flares without enhanced VHE activity in 2006–2007 (Tagliaferri et al. 2008), 2015 August–2016 January (Kapanadze et al. 2016a), etc., there was a lack of a correlated X-ray–TeV variability also in the period presented here. Although 1ES 1959+650 was observed intensively with the FACT during most of Periods 1a–1b and 2a–2c, it did not show significant variability, as opposed to the strong flaring activity at X-rays. Consequently, the source did not show a two-humped structure in the log ν–$F_{\rm var}$ plane (with the quantity $F_{\rm var}$ calculated from the available data series in each spectral band during the entire period), which is a typical feature of HBLs and explained as resulting from the correlation between the synchrotron and IC peaks, as well as demonstrating that the electron energy distribution is most variable at the highest energies (according to one-zone SSC scenarios; Furniss et al. 2015). The log ν–$F_{\rm var}$ plane shows the synchrotron peak with the highest variability in the 2–10 keV band in the log ν–$F_{\rm var}$ plane (due to frequent detection of the synchrotron SED peak at hard X-rays), and Table 8 presents a general trend of increasing fractional amplitude from optical to X-ray bands (except for some exclusions in the UVOT bands). A VHE "inactivity" of the source can be related to the upscatter of BAT-band photons to VHE frequencies in the K-N regime, yielding a severe decrease in the produced TeV emission with diminished variability due to the K-N suppression and very low, insignificantly variable BAT-band emission in 1ES 1959+650. On the contrary, the source showed contemporaneous fast, strong X-ray and VHE flares (with a few exceptions) in 2016 June–July (Kapanadze et al. 2018a), which could be related to the efficient upscatter of X-ray photons to the TeV

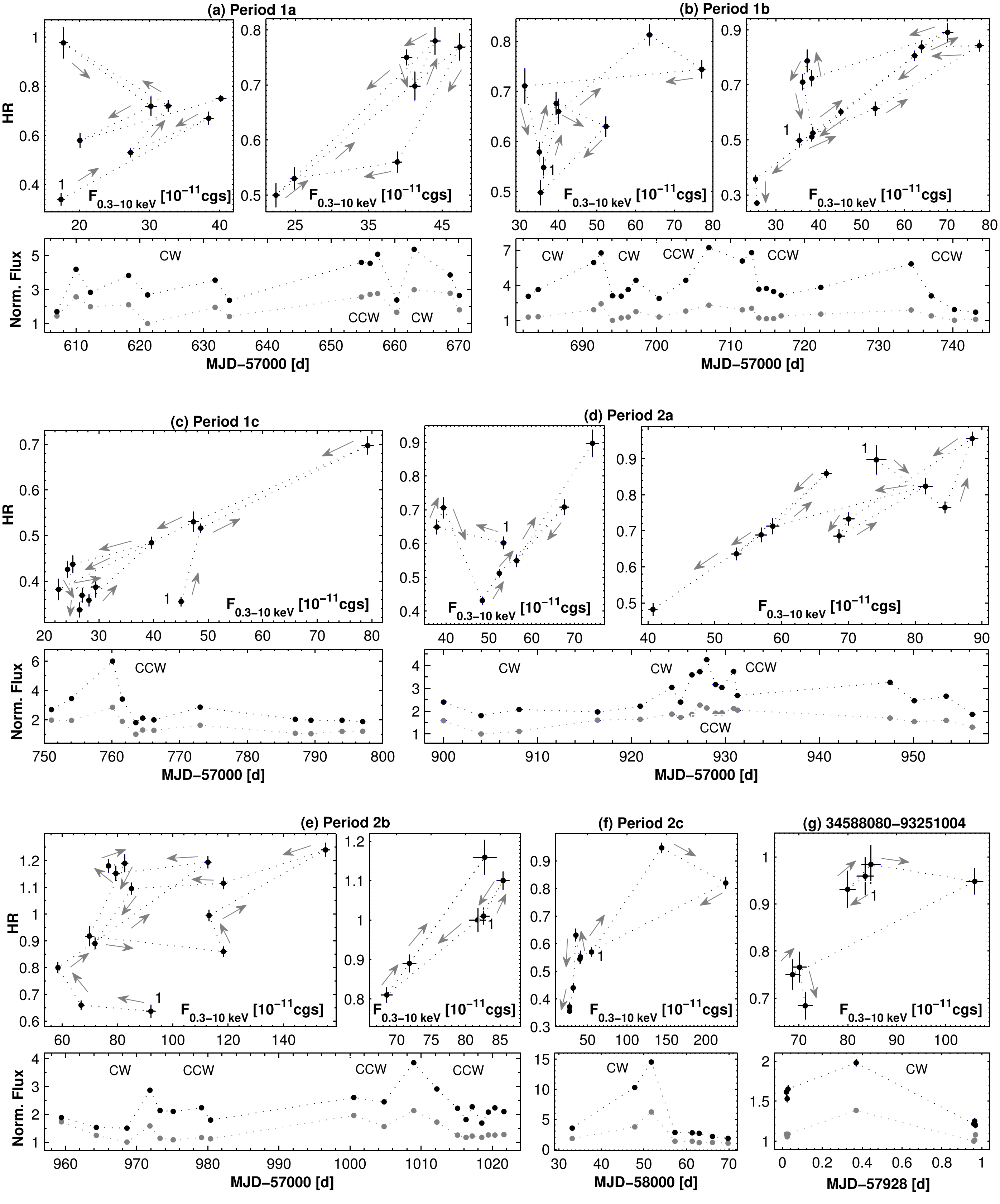

Figure 12. Spectral hysteresis in different epochs, along with the normalized soft 0.3–2 keV (gray circles) and hard 2–10 keV (black circles) fluxes plotted vs. time. The light curves for hard fluxes are shifted arbitrarily for a better resolution. In each plane, the start point is denoted by “1.” Gray arrows show the direction of increasing time, and the data points corresponding to the subsequent XRT observations are connected with a dotted line. The acronym “cgs” stands for erg cm^{-2} s^{-1}.

Table 11
Summary of CW and CCW Loops Shown by 1ES 1959+650 in the HR–Flux Plane

Figure	MJD	X-Ray Variability Instance
		CW Evolution
12(a), panel 1	57607.0–57634.1	Low-amplitude flaring activity in the first half of Period 1a (Figure 5(a))
12(a), panel 2	57654.7–57660.3	The second fast flare in the second half of Period 1a (Figure 5(a))
12(b), panel 1	57682.7–57700.4	The first two fast flares in Period 1b (Figure 5(b))
12(d), panel 1	57900.0–57928.0	Brightness decline and the subsequent flare in Period 2a (Figure 5(d))
12(e), panel 1	57959.4–57965.2	Brightness increase in the start of Period 2b (Figure 5(e))
12(f)	58033.1–58057.3	An X-ray flare in Period 2c (Figure 5(f))
12(g)	57928.0–57928.9	An IDV on 2017 Jun 24 (Figure 7(a),panels 6–8)
		CCW Evolution
12(a),Panel 2	57654.7–57660.3	The first fast flare in the second half of Period 1a (Figure 5(a))
12(b),Panel 2	57700.4–57740.2	The third and last flares in Period 1b (Figure 5(b))
12(c)	57754.0–57794.0	The strong and low-amplitude flares in Period 1c (Figure 5(c))
12(d), Panel 2	57928.0–57931.0	Low-amplitude flare superimposed on a long-term one in the middle of Period 2a (Figure 5(d))
12(e), Panels 1–2	57965.2–58022.0	The first and second flares in Period 2b (Figure 5(e))

energy range in the Thomson regime. We conclude that the $\log \nu$–$F_{\rm var}$ plane also shows a requirement that the emission models be more complex than a simple one-zone SSC scenario in the period presented here.

Using the available TeV and simultaneous MWL spectral data of 1ES 1959+650 for broadband SED construction, different authors adopted complicated models to obtain a satisfactory fit. Krawczynski et al. (2004) postulated a second, dense electron population within a small emission region to fit the SED belonging to the epoch of the "orphan" TeV flare in 2002. Aliu et al. (2013) used a combined SSC+EC model and the three SEDs obtained during 2007–2011 with VERITAS and other simultaneous MWL observations. For the SEDs corresponding to the low and high VHE states of the source detected with VERITAS, Aliu et al. (2014) adopted a one-zone SSC scenario with variable Doppler factor. Patel et al. (2018) modeled six optical-HE SEDs of 1ES 1959+650 using a two-zone SSC scenario. Along with performing intensive ToO observations of our target with *Swift* and monitoring its VHE behavior with the FACT telescope, we plan to extract the TeV-band spectral points from the FACT detections with a high significance[19] and to model a broadband SED from different epochs using various emission scenarios (forthcoming paper).

Although the source exhibited a general enhanced HE state during 2015 August–2017 November (similar to the X-ray energy range), no LA-band flares were observed along with some X-ray ones, or showed a significant offset. As a result, the contemporaneous 0.3–10 keV and 0.3–100 GeV fluxes from this period do not show a correlation (Figure 11(C)), in contrast to those from the observations performed in 2016 February–July (Kapanadze et al. 2018a). Moreover, the sources exhibited a positive correlation between the LAT- and UVOT-band fluxes in Period 1 (see Figure 11(Da) and Table 7), which can be explained via the effect of the K-N suppression in the IC process, leading to the UV photons being upscattered most efficiently at the MeV–GeV energies by the electrons radiating in the X-ray (Tramacere et al. 2009).

The source showed new highest historical states in the UVOT optical–UV bands (in Periods 1 and 2, respectively), although its flaring activity was not as strongly enhanced in this energy range since 2015 as it happened in the XRT and LAT bands. Note that the source showed comparable optical–UV states also in 2012, when it did not show strong X-ray and γ-ray activities. A similar situation was observed also during the long-term 15 GHz program with the OVRO telescope.

The UVOT-band fluxes showed a weak anticorrelation with the 0.3–10 keV flux during 2016 August–2017 November (see Figure 11(B)), which can be explained through a hardening in the electron energy distribution, shifting the entire synchrotron bump to higher energies, leading to a brightness decline at lower frequencies while the X-ray brightness is rising (see Aleksic et al. 2015; Kapanadze et al. 2017). Our finding of a positive $E_{\rm p}$–$F_{0.3-10\,{\rm keV}}$ correlation (see Section 3.3), i.e., a shift of the synchrotron SED peak toward higher energies with increasing X-ray flux, is in favor of this suggestion. Note that the shift of the peak of electron energy distribution with the increasing brightness was yielded by the simulations of Katarzynski et al. (2006) in the framework of the stochastic acceleration of electrons with a narrow initial energy distribution, having an average energy significantly higher than the equilibrium energy. Nevertheless, the aforementioned anticorrelation is shown by only a subset of the data belonging to Period 2, which was characterized by the features of efficient stochastic acceleration (see Figure 11(Bc) and Section 5.1). In contrast, an anticorrelation between the XRT- and UVOT-band fluxes was not observed in Period 1 (see Figure 11(Bb)), which was characterized by possibly less efficient stochastic acceleration. Note that the 0.3–10 keV emission sometimes showed a very fast variability on intraday timescales, which was not observed at the optical–UV frequencies (owing to the position of the synchrotron SED peak at significantly higher frequencies; see Costamante et al. 2018). This difference also could contribute to the weakness or absence of the correlation between the XRT and UVOT-band emissions.

The optical–UV fluxes from the UVOT observations showed a strong or very strong correlation to each other in all periods, demonstrating their origin from the same electron population (similar to previous years; see Table 7 and Figure 11). Similar to Zhang & Li (2017), we have checked the source for the possible optical "bluer-when-brighter" chromatism. This trend was not evident in the case of the adjacent bands (Figure 13(a)) and weakly presented in the plane U–V versus U with the Spearman coefficient $\rho = 0.34 \pm 0.12$ (Figure 13(b)). The

---

[19] The software for the extraction of the linear VHE flux and spectral points is under development.

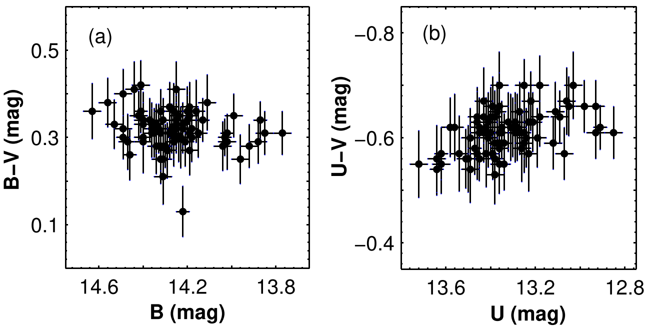

Figure 13. Color–magnitude diagrams for the observations performed with the UVOT.

latter can be treated as the lower-energy tail of a significantly stronger "harder-when-brighter" spectral trend in the 0.3–10 keV energy range, demonstrating a stronger and faster variability in the number of the electrons producing X-ray photons via the synchrotron mechanism. Note that the "bluer-when-brighter" chromatism was stronger during the ground-based optical observations of the source in 2010–2016 (evident even for the adjacent bands; Zhang & Li 2017).

Although the 15 GHz observations showed an elevated radio state along some strong X-ray flares, we have not found a significant correlation of the OVRO-band flux with that from the XRT or other spectral bands, possibly due to the contributions from different jet areas.

6. Summary

In this paper, we have presented the spectral and timing results obtained during the intensive *Swift* observations of the TeV-detected blazar 1ES 1959+650 during 2016 August–2017 November. The main results of this study are as follows:

1. The source continued its trend of gradually enhancing X-ray flaring activity in the 0.3–10 keV energy range that started in 2015 August, possibly caused by the long-term increase in the collimation rate of high-energy plasma through the jet. In the present period, a new highest historical X-ray state was recorded twice, and 1ES 1959+650 was the brightest blazar in the 0.3–10 keV energy range during some time intervals. A general higher state was accompanied by low-amplitude or strong flares by factors of 1.7–3.5, lasting from several days to a few weeks. Moreover, we detected 32 instances of the 0.3–10 keV IDV with several occasions of the extremely fast brightness fluctuations by fractional amplitudes of 5.4%–7.5% within 1 ks exposures, which possibly were generated by the smallest-size jet turbulent structures with strongest magnetic field. The source showed the fastest flux halving in 1.3 days, and this instance could be caused by the transition of the relativistic shock front from the area with highly developed turbulence (and having stronger magnetic field) into that with lower turbulence and weaker magnetic field, yielding a halving in the number of the emitted X-ray photons.
2. The 2016 August–2017 November period was characterized by a lack of correlation between the X-ray and VHE fluxes, with nonvariable, low-state TeV emission along with enhanced 0.3–10 keV flaring activity, and hinting at the possibility that the VHE emission arose from the jet area, which was more complex than a single zone. The *Fermi*-LAT observations found the source in an elevated HE state during the period presented here, and the 0.3–100 GeV emission showed its highest historical value with 2-week bins, exceeding a level of 10^{-7} photons cm^{-2} s^{-1} for the first time in the LAT operations. Similarly, the source attained its highest optical–UV fluxes in the UVOT optical–UV bands and showed an anticorrelation with the 0.3–10 keV emission, which is expected in the case of the stochastic acceleration of electrons with a narrow initial energy distribution, having an average initial energy significantly higher than the equilibrium energy. The fractional variability amplitude from the MWL data series showed an increase from radio to X-ray frequencies, reaching its maximum for the 2–10 keV flux and indicating the maximum variability in that part of the electron energy distribution, which is responsible for a photon generation in this energy range. However, no clearly expressed higher-energy peak was observed in the $\log\nu - F_{\rm var}$ plane (familiar to HBL sources), indicating a requirement that the emission models be more complex than one-zone SSC scenarios.
3. Along with a strong flux variability, the source also showed an extreme spectral behavior. The 0.3–10 keV spectra generally showed their best fits with the log-parabolic model, yielding a very wide range of the curvature parameter $b = 0.10(0.05)$–$0.83(0.12)$ and photon index at 1 keV $a = 1.55(0.03)$–$2.41(0.03)$. The position of the synchrotron SED peak showed an extreme variability on various timescales between energies less than 0.2 keV and 7.7 ± 0.7 keV, with 28% of the spectra peaking at hard X-rays during the X-ray flares and six spectra with $E_{\rm p} > 5$ keV. The synchrotron SED showed a positive correlation with the 0.3–10 keV flux, shifting by several keV to higher energies during the flaring phases, and moved back with a brightness drop. However, it underwent a very fast increase by 4.4 keV and a subsequent decline by 5.2 keV within 2 days, while the 0.3–10 keV flux did not show a significant variability. The photon index generally followed a "harder-when-brighter" trend (except for some short time intervals with the opposite trend, possibly related to the emergence of a new soft X-ray component), with the largest hardenings by $\Delta a = 0.56$–0.67 in 11–18 days and softenings by $\Delta a = 0.50$–0.56 in 6–8 days. During 2017 May–November, the source mostly showed a relatively small X-ray spectral curvature and an anticorrelation with the position of the SED peak (in contrast to the previous period), expected in the case of efficient stochastic acceleration of X-ray-emitting electrons from magnetic turbulence close to the shock front propagating through the jet. For the whole 2016 August–2017 November period, the source showed a positive correlation between the curvature parameter and photon index, expected in the case of an EDAP process (a particular case of the first-order Fermi mechanism), although this correlation was very weak, possibly as a result of the "competition" with the other types of acceleration mechanisms, e.g., stochastic acceleration and cooling processes.
4. Moreover, our target sometimes showed very hard X-ray and HE spectra with a photon index smaller than 1.70, whose origin can be explained more easily in the framework of hadronic scenarios than within the leptonic models. Nevertheless, the source showed a significantly

harder 2–300 GeV photon index compared to its lower-energy (0.3–2 GeV) "counterpart," which could be caused by the hadronic contribution to higher-energy LAT-band emission. Evidences for hadrons make 1ES 1959+650 a potential source of VHE cosmic rays.

5. Our study of spectral hysteresis patterns revealed that short-term flares and extreme spectral variability in the presented period were related to a complex and variable interplay between the acceleration and cooling timescales of emitting particles and flux variability timescale. Some 0.3–10 keV flares showed patterns inherent to the rapid injection of very energetic particles and dominance of synchrotron cooling with a possible soft lag, while other flares demonstrated a gradual acceleration and dominance of particle escape effects in the brightness decline phase.

B.K. and L.T. thank the Shota Rustaveli National Science Foundation and Ilia State University for grant FR/377/6-290/14. P.R. acknowledges contract ASI-INAF I/004/11/0. This research has made use of the `XRTDAS` software, developed under the responsibility of the ASDC, Italy, and data from the OVRO 40 m monitoring program, which is supported in part by NASA grants NNX08AW31G and NNX11A043G and NSF grants AST-0808050 and AST-1109911. We thank the FACT collaboration for making their analysis results publicly available. This research has made use of data from the MOJAVE database, which is maintained by the MOJAVE team (Lister et al. 2011), and the MAXI data provided by RIKEN. We thank the anonymous referee for his/her useful comments that helped to improve the paper's quality.

ORCID iDs

B. Kapanadze https://orcid.org/0000-0002-7146-6751
S. Vercellone https://orcid.org/0000-0003-1163-1396
P. Romano https://orcid.org/0000-0003-0258-7469
P. Hughes https://orcid.org/0000-0002-0691-3041
M. Aller https://orcid.org/0000-0003-2483-2103
M. Reynolds https://orcid.org/0000-0003-1621-9392

References

Abdo, A. A., Ackermann, M., Ajello, M., et al. 2011, ApJ, 727, 129
Aleksic, J., Ansoldi, S., Antonelli, L. A., et al. 2015, A&A, 576, 176
Aliu, E., Archambault, S., Arlen, T., et al. 2013, ApJ, 775, 3
Aliu, E., Archambault, S., Arlen, T., et al. 2014, ApJ, 797, 89
Anderhub, H., Backes, M., Biland, A., et al. 2013, JInst, 8, P06008
Atwood, W. B., Abdo, A. A., Ackermann, M., et al. 2009, ApJ, 697, 1071
Barthelmy, S. D., Berbier, L. M., Cummings, J. R., et al. 2005, SSRv, 120, 143
Burrows, D. N., Hill, J. E., Nousek, J. A., et al. 2005, SSRv, 120, 165
Costamante, L., Bonnoli, G., Tavecchio, F., et al. 2018, MNRAS, 477, 4257
Cui, W. 2004, ApJ, 605, 662
Dermer, C. D., Schlickeiser, R., & Mastichiadis, A. 1992, A&A, 256, L27
Dorner, D., Ahnen, M. L., Bergmann, M., et al. 2015, arXiv:1502.02582
Falcone, A., Cui, W., & Finley, J. P. 2004, ApJ, 601, 165
Falomo, R., Pian, E., & Treves, A. 2014, A&ARv, 22, 37
Fumagalli, M., Dessauges-Zavadsky, M., Furniss, A., et al. 2012, MNRAS, 424, 2276
Furniss, A., Fumagalli, M., Falcone, A., & Williams, D. A. 2013, ApJ, 770, 109
Furniss, A., Noda, K., Boggs, S., et al. 2015, ApJ, 812, 65
Gehrels, N., Chincarini, G., Giommi, P., et al. 2004, ApJ, 611, 1005
Graff, P., Georganopoulos, M., Perlman, E. S., & Kazanas, D. 2008, ApJ, 689, 68
Kalberla, P. M. W., Burton, W. B., Hartman, D., et al. 2005, A&A, 440, 775
Kapanadze, B., Dorner, D., Romano, P., et al. 2017, ApJ, 848, 103
Kapanadze, B., Dorner, D., Romano, P., et al. 2018a, MNRAS, 473, 2542
Kapanadze, B., Dorner, D., Vercellone, S., et al. 2016a, MNRAS, 461, L26
Kapanadze, B., Romano, P., Vercellone, S., et al. 2016b, MNRAS, 457, 704
Kapanadze, B., Vercellone, S., Romano, P., et al. 2018b, ApJ, 854, 66
Kapanadze, B., Vercellone, S., Romano, P., et al. 2018c, ApJ, 858, 68
Katarzynski, K., Ghisellini, G., Mastichiadis, A., Tavecchio, F., & Maraschi, L. 2006, A&A, 453, 47
Kaur, N., Chandra, S., Baliyan, K. S., & Sameer, G. S. 2017, ApJ, 846, 158
Kirk, J. G., & Mastichiadis, A. 1999, APh, 11, 45
Krawczynski, H., Hughes, S. B., Horan, D., et al. 2004, ApJ, 601, 151
Krimm, H., Holland, S. T., Corbet, R. H. D., et al. 2013, ApJ, 209, 14
Landau, R., Golisch, B., Jones, T. J., et al. 1986, ApJ, 308, 78
Lister, M. L., Aller, H. D., Aller, M. F., et al. 2011, AJ, 137, 3718
Mannheim, K. 1992, A&A, 269, 67
Marscher, A. P., & Gear, W. K. 1985, ApJ, 298, 114
Massaro, E., Perri, M., Giommi, P., & Nesci, R. 2004, A&A, 413, 489
Massaro, F., Paggi, A., & Cavaliere, A. 2011a, ApJL, 742, L32
Massaro, F., Paggi, A., Elvis, M., & Cavaliere, A. 2011b, ApJ, 739, 73
Matsuoka, M., Kawasaki, K., Ueno, S., et al. 2009, PASJ, 61, 999
Mizuno, Y., Pohl, M., Niemiec, J., et al. 2014, MNRAS, 439, 3490
Mücke, A., Protheroe, R. J., Engel, R., Rachen, J. P., & Stanev, T. 2003, Aph, 18, 593
Padovani, P., & Giommi, P. 1995, ApJ, 444, 567
Pandey, A., Gupta, A. C., & Wiita, P. 2017, ApJ, 841, 123
Patel, S. R., Shukla, A., Chitnis, V. R., et al. 2018, A&A, 611, 44
Richards, J. L., Max-Moerbeck, W., Pavlidou, V., et al. 2011, ApJS, 194, 209
Roming, P. W. A., Kennedy, T. E., Mason, K. O., et al. 2005, SSRv, 120, 95
Shukla, A., Chitnis, V. R., Singh, B. B., et al. 2015, ApJ, 798, 2
Sokolov, A., Marscher, A. P., & McHardy, I. M. 2004, ApJ, 613, 725
Tagliaferri, G., Foschini, L., Ghisellini, G., et al. 2008, ApJ, 679, 1029
Tramacere, A., Giommi, P., Perri, M., Verrecchia, F., & Tosti, G. 2009, A&A, 501, 879
Tramacere, A., Massaro, E., & Taylor, A. M. 2011, ApJ, 739, 66
Vaughan, S., Edelson, R., Warwick, R. S., & Uttley, P. 2003, MNRAS, 345, 1271
Virtanen, J. J. P., & Vainio, R. 2005, ApJ, 621, 313
Zhang, Y.-H., & Li, J.-C. 2017, MNRAS, 469, 1682